



Orbital Elements and Individual Component Masses from Joint Spectroscopic and Astrometric Data of Double-line Spectroscopic Binaries*

Jennifer Anguita-Aguero¹, Rene A. Mendez¹ , Rubén M. Clavería², and Edgardo Costa¹

¹Astronomy Department, Universidad de Chile, Casilla 36-D, Santiago, Chile; rmendez@uchile.cl

²Department of Engineering, University of Cambridge, Cambridge, UK

Received 2021 August 26; revised 2021 December 16; accepted 2021 December 31; published 2022 February 8

Abstract

We present orbital elements, orbital parallaxes, and individual component masses for 14 spatially resolved double-line spectroscopic binaries derived doing a simultaneous fit of their visual orbit and radial velocity curve. This was done by means of a Markov Chain Monte Carlo code developed by our group that produces posterior distribution functions and error estimates for all of the parameters. Of this sample, six systems had high-quality previous studies and were included as benchmarks to test our procedures, but even in these cases, we could improve the previous orbits by adding recent data from our survey of southern binaries being carried out with the HRCam and ZORRO speckle cameras at the SOAR 4.1 m and Gemini South 8.1 m telescopes, respectively. We also give results for eight objects that did not have a published combined orbital solution, one of which did not have a visual orbit either. We could determine mass ratios with a typical uncertainty of less than 1%, mass sums with uncertainties of about 1%, and individual component masses with a formal uncertainty of $0.01 M_{\odot}$ in the best cases. A comparison of our orbital parallaxes with available trigonometric parallaxes from Hipparcos and Gaia eDR3 shows a good correspondence, the mean value of the differences being consistent with zero within the errors of both catalogs. We also present observational H-R diagrams for our sample of binaries, which, in combination with isochrones from different sources, allowed us to assess their evolutionary status and the quality of their photometry.

Unified Astronomy Thesaurus concepts: [Binary stars \(154\)](#); [Astrometric binary stars \(79\)](#); [Spectroscopic binary stars \(1557\)](#); [Stellar masses \(1614\)](#); [Trigonometric parallax \(1713\)](#); [Stellar distance \(1595\)](#); [Astrometry \(80\)](#); [Speckle interferometry \(1552\)](#); [Radial velocity \(1332\)](#); [Markov chain Monte Carlo \(1889\)](#)

1. Introduction


Binary stars are powerful laboratories to test various aspects of stellar astrophysics because they enable to us to access a key but elusive parameter that dictates the structure and evolution of stars: their mass. In combination with Kepler's laws, the observation of binary systems allows one to directly determine the masses of stars. Indeed, the most fundamental parameter determining the internal structure and evolutionary path of stars of a given chemical composition is their initial mass, as shown by the well-known Vogt–Russell theorem (Kahler 1972; Kippenhahn et al. 2012; for a general review, see Massey & Meyer 2001; and the textbooks by Iben 2012 for details of the physical models). This theoretical prediction is, however, not

straightforward to test due to the limited number of stars with well-known individual masses.

Kepler's laws give us the way to directly determine the mass of a stellar system by studying the motion of stars that are bound by their mutual gravitational attraction, i.e., binary stars (Pourbaix 1994). Considering that roughly half of the solar-type stars in the solar neighborhood belong to binary systems (Raghavan et al. 2010; Duchêne & Kraus 2013; Fuhrmann et al. 2017), in principle, it is possible to determine precise masses for a very large number of stars. Gravitational microlensing might eventually become another potentially very precise method for mass determination (Ghosh et al. 2004; Gould 2014), but so far, it has been restricted to a few cases (Bennett et al. 2020; Wyrzykowski & Mandel 2020). Circumstellar disks around young stars (Pegues et al. 2021) are also becoming a viable and promising method. In the case of microlensing events, the mass of the lens can be determined only in limited cases, because it requires a knowledge of both the source and lens distances, as well as their relative proper motions. The second method relies on the existence of a purely Keplerian disk,³ i.e., in a steady-state configuration and not subject to magnetohydrodynamical effects, which enables a purely dynamical mass determination. In the case of visual binary stars, the subject of this paper, a mass determination requires a determination of the so-called orbital elements that completely define the projected orbit in terms of the true intrinsic orbital parameters.

One of the main relationships reflecting the dependency on mass of the star's properties is the mass–luminosity relation

* Based in part on observations obtained at the international Gemini Observatory, a program of the NSF's NOIRLab, which is managed by the Association of Universities for Research in Astronomy (AURA) under a cooperative agreement with the National Science Foundation on behalf of the Gemini Observatory partnership: the National Science Foundation (United States), National Research Council (Canada), Agencia Nacional de Investigación y Desarrollo (Chile), Ministerio de Ciencia, Tecnología e Innovación (Argentina), Ministério da Ciência, Tecnologia, Inovações e Comunicações (Brazil), and Korea Astronomy and Space Science Institute (Republic of Korea). Based also in part on observations obtained at the Southern Astrophysical Research (SOAR) telescope, which is a joint project of the Ministério da Ciência, Tecnologia, e Inovações (MCTI) da República Federativa do Brasil, the U.S. National Optical Astronomy Observatory (NOAO), the University of North Carolina at Chapel Hill (UNC), and Michigan State University (MSU).

 Original content from this work may be used under the terms of the [Creative Commons Attribution 4.0 licence](#). Any further distribution of this work must maintain attribution to the author(s) and the title of the work, journal citation and DOI.

³ Usually found only on young stars.

(MLR), first discovered empirically in the early 20th century and later explained on theoretical grounds (Eddington 1924). Improving the observational MLR is not a simple task, because it involves determining not only precise masses but also another elusive parameter, distance, by means of trigonometric parallaxes. To complicate things further, the observational MLR has a statistical dispersion that cannot be explained exclusively by observational errors in the luminosity or mass; there seems to be an intrinsic dispersion caused by differences in age and/or chemical composition from star to star. Currently, the best MLRs for main-sequence stars are those of Torres et al. (2010) and Benedict et al. (2016), but neither of them include low-metallicity stars (e.g., only one with $[\text{Fe}/\text{H}] < -0.25$ in Torres et al. 2010). Other studies, using long-baseline optical interferometry of binary systems, have begun to address metallicity (e.g., Boyajian et al. 2012a, 2012b; Feiden & Chaboyer 2012) but have reached only as low as about $[\text{Fe}/\text{H}] = -0.5$. For a recent study of the effects of metallicity on the MLR for $M < 0.7 M_{\odot}$, see Mann et al. (2019). Our own speckle survey, described below, is focusing, in part, precisely on low-metallicity objects, following the pioneer study of Horch et al. (2015b, 2019a).

The recent advent of the Gaia satellite (Luri et al. 2018) has dramatically improved the precision of stellar distances within the solar neighborhood. Up to a distance of 250 pc, well beyond what it is usually adopted as the “radius” of the solar neighborhood, a parallax determined by Gaia has an uncertainty under 1%, which by current standards would have basically solved the distance dilemma in the MLR. Despite this promising scenario, much remains to be done to increase the number of stars with well-known masses because of the relative lack of high-precision orbits for binary systems. On the other hand, the Gaia satellite faces observational difficulties at resolving systems close to its angular resolution limit. It is well known that the Hipparcos parallaxes were indeed biased due to the orbital motion of the binary (i.e., the parallax and orbit signal are blended), as shown by Söderhjelm (1999; see, in particular, Section 3.1 and Table 2), and it is likely that Gaia will suffer from a similar problem.⁴

A good starting point for systematic surveys to determine stellar masses are all-sky catalogs that include identification of confirmed or suspected visual binaries, such as the Hipparcos catalog (Lindegren et al. 1997), as well as the more recent Gaia discoveries (Kervella et al. 2019; Brandt 2021; El-Badry et al. 2021), or spectroscopic binaries, such as the Geneva–Copenhagen spectroscopic survey (Nordström et al. 2004). To this end, in 2014, we initiated a systematic campaign to complete or improve the observation of southern binaries mainly from the above catalogs (Mendez et al. 2018) using the high-speed speckle camera HRCam at the Southern Astrophysical Research (SOAR) 4.1 m telescope (Tokovinin & Cantarutti 2008; Tokovinin 2018); several publications have resulted from this effort, including Gomez et al. (2016), Mendez et al. (2017), Claveria et al. (2019), Docobo et al. (2019), Gómez et al. (2021), Mendez et al. (2021), and Villegas et al. (2021). Considering that metal-poor binary systems are typically farther away and therefore fainter and/or more

compact spatially, making them difficult objects for optical interferometry with 4 m or smaller telescopes, in 2019, we also started a program focused on these very systems with the ZORRO Speckle Camera of the Gemini South 8.1 m telescope at Cerro Pachón.⁵ We note that southern binaries are currently being monitored systematically only by our team, which makes our speckle survey unique. Complementarity with Gaia is a very strong reason to carry out a survey of nearby binaries now; during each observation, Gaia is not expected to resolve systems closer than about $0''.4$, though over the mission, there will be a final resolution of $0''.1$. This is shown graphically in Figure 1 from Ziegler et al. (2018), where the current resolution of the second Gaia data release is shown to be around $1''$, being a function of the magnitude difference between primary and secondary.⁶

For many years, exoplanet searches excluded binary systems, but nowadays, more than 200 planets have been discovered in them,⁷ representing a multiplicity rate of about 23% for hosts to exoplanets across all spectral types (Fontanive & Bardalez Gagliuffi 2021). Initially, they were discovered serendipitously, like Gliese 86 Ab (Queloz et al. 2000) and γ Cep Ab (Hatzes et al. 2003), but more recently, they have been discovered as part of dedicated imaging, transit, and radial velocity (RV) surveys (e.g., see Fontanive & Bardalez Gagliuffi 2021). Given that the formation of stars in multiple systems is a frequent by-product of stellar formation, a current open question is to understand how the presence of a stellar companion can affect the planetary formation process. For years, planetary formation theories have been restricted to the case of a single-star environment to understand the formation of our own solar system (Mordasini et al. 2008). For the most frequent dynamical configuration observed for planet(s) in binaries (see the classification by Dvorak 1982), the S-type circumprimary one with a planet orbiting one component of the binary, generally the most massive one, the models predict that the presence of a very close binary companion can truncate a protoplanetary disk, hence obstructing the formation of a planet by core accretion or ejecting the planet in unstable systems (Thebault & Haghighipour 2015). Dedicated observing campaigns confirmed that short- and intermediate-separation (≤ 300 au) binaries have a statistically lower chance of hosting planets or brown dwarf companions, and that wide binaries, on the contrary, have no influence on the architectures of planetary systems (Matson et al. 2018). This effect seems to also be corroborated by the study of young stars for which short-separation (≤ 100 au) binaries have a lower probability of hosting circumstellar dust in the innermost few au around each star, therefore having a depleted reservoir of solids for the formation of planets by core accretion (Duchêne 2010).

Among different types of binary systems, spatially resolved double-line spectroscopic binaries (hereafter SB2s) with known RV curves are particularly important. If their RV curves can be combined with their astrometric orbits, it is possible to obtain a

⁵ See <https://www.gemini.edu/instrumentation/current-instruments/alopeke-zorro>.

⁶ It is expected that, from the third Gaia data release on, the treatment of binary stars will be much improved by incorporating orbital motion (and its impact on the photocenter position of unresolved pairs) into the overall astrometric solution, thus significantly suppressing/alleviating the parallax bias; this, in turn, calls precisely for having good orbital elements for these binaries, which is one of the secondary goals of our project.

⁷ As of 2021 November 3, 217 planets were known in 154 binary systems (<https://www.univie.ac.at/adg/schwarz/multiple.html>).

⁴ For example, according to Tokovinin’s multiple star catalog, HIP 64421 contains a binary with a 27 yr orbit. Its Hipparcos parallax is 8.6 mas, its dynamical parallax is 8.44 mas, and its Gaia DR2 parallax is 3 mas. However, Gaia does give a consistent parallax for the C component at $1''.9$: 9.7 ± 0.3 mas; see <http://www.ctio.noao.edu/~atokovin/stars/>. There are other examples like this in the cited catalog.

complete and unambiguous solution for the orbital elements, as well as individual component masses, with high precision (Mendez et al. 2017, 2021). With high-quality data in hand, it is also possible to derive parallax-free distances—the so-called orbital parallaxes—for these systems, which are derived from the ratio of the semimajor axes (Docobo et al. 2018b; Piccotti et al. 2020). Orbital parallaxes are completely independent of the trigonometric parallax and thus allow an assessment of Gaia’s parallaxes (Pourbaix 2000; Mason 2015). Furthermore, increasing the sample of well-studied SB2s is important because, statistically, the mass-ratio distribution of these binaries—a parameter assumed to be frozen since their formation but observationally retrievable—has an important imprint from the initial mass function, as shown by, e.g., the simulations by Ducati et al. (2011). This traditional vision is, however, being somewhat challenged by more recent simulations that demonstrate that high-mass stars can capture lower-mass stars with luminosities far smaller than those of their host during the first few million years of star cluster evolution (Wall et al. 2019). Additionally, N -body simulations that incorporate magnetohydrodynamic effects have shown that dynamical interactions between stars in the presence of gas during cluster formation can modify the initial mass-ratio distribution toward binaries with a larger mass difference (Cournoyer-Cloutier et al. 2021).

Unfortunately, and despite sustained efforts to monitor SB2s (see, e.g., Halbwegs et al. 2020 and their series of papers), the number of systems for which both an RV curve and a precise astrometric orbit are available is still rather small. In this paper, we contribute to alleviating this situation by determining combined orbits for 14 SB2 systems, some of which have been observed during our SOAR speckle survey of southern binary stars (Mendez et al. 2018) and for which there are complementary published data as well.

Methodologically, the most common procedure is to solve the astrometric visual orbit separately from the RV curve. In this approach, the amplitude ratio between the RV curves of the primary and secondary gives an estimation of the mass ratio, while the astrometric orbit gives the mass sum (assuming a parallax). This is most often done when the primary and secondary amplitudes are not well determined, e.g., when the spectral resolution prevents full deblending of the spectral lines of both components (see, e.g., Tokovinin & Latham 2017), or in the case of single-line spectroscopic binaries with a visual orbit (see, e.g., Docobo et al. 2018c). In both cases, it is not possible to directly link the RV curve to the astrometric orbit in a self-consistent manner. On the other hand, if the visual orbit and velocity amplitudes are believed to be reliable, it is possible to determine a simultaneous solution and, in the process, determine the orbital parallax based solely on the orbital motion of the pair. Both scenarios are thoroughly explained, including graphical flowcharts, in Villegas et al. (2021, Section 4.2), while in Appendix A of Mendez et al. (2017), we provide a detailed step-by-step flow of our calculations. In this work, well-measured RV curves and visual orbits are available for most systems, so by adopting the latter of these schemes, we were able to determine orbital parallaxes for the majority of our binaries.

This paper is organized as follows. In Section 2, we introduce our list of SB2s, together with their basic photometric properties. In Section 3, we present the results of our orbital calculations and individual component masses. These results, along with the photometry, are presented on Hertzsprung–

Russell (H-R) diagrams in Section 4, while in Section 5, we describe our sample on an object-by-object basis. Finally, in Section 6, we present the main conclusions of our study.

2. Basic Properties of the Binary Systems

To select the sample for the present work, we started by doing a cross-match between the Sixth Catalog of Orbits of Visual Binary Stars (hereafter Orb6⁸) maintained by the US Naval Observatory and the 9th Catalog of Spectroscopic Binary Orbits (hereafter SB9;⁹ Pourbaix et al. 2004). Orb6 is the most comprehensive catalog of binary systems with published orbital elements, and SB9 contains RV amplitudes for all binary systems for which it has been possible to fit an RV curve. Having identified those systems confirmed as SB2s in SB9, we pinpointed the binaries for which a combined astrometric/RV study of the orbit was not available in the literature by means of the notes and comments given in Orb6 and SB9. This led to an initial working list of 17 binary systems.

For the systems selected as indicated above, we retrieved their RV data from SB9 or references provided therein, astrometric data from the US Naval Observatory Fourth Catalog of Interferometric Measurements of Binary Stars,¹⁰ and historical astrometry included in the Washington Double Star Catalog (WDS) effort (Mason et al. 2001; kindly provided to us by Dr. Brian Mason from the US Naval Observatory). Finally, we included recent results obtained with the HRCam speckle camera at the SOAR 4.1 m telescope as part of our monitoring of southern binaries described in Mendez et al. (2017). Examination of the information collected showed that only 14 of the systems in our starting list had sufficient data to warrant further analysis. We must emphasize that, as a result of our selection process, our final sample is very heterogeneous, and it is not complete or representative in any astrophysical sense. From this point of view, the main contribution of this paper is the addition of new orbits and individual component masses for this type of binary. In our final list, we also included a few previously studied objects in order to test our procedures and compare results. When available, we added SOAR+HRCam astrometric measurements we secured after the publication of their last orbit determination to improve the solution.

Table 1 presents the basic properties available in the literature for the sample studied in this paper. The first three columns give the name in the WDS (and below it, its corresponding HD number), the discoverer designation code assigned in the WDS to each target used throughout the paper, and the sequential number in the Hipparcos catalog. The fourth column gives the apparent V magnitude for the system as listed in SIMBAD (V_{SIMBAD} ; Wenger et al. 2000). The fifth and sixth columns present the V magnitude given in the Hipparcos catalog (V_{Hip}) and its source, respectively. The seventh and eighth columns list the color ($(V - I)_{\text{Hip}}$) and its source, respectively, also from the Hipparcos catalog. The ninth and 10th columns give the V magnitudes for the primary (V_A) and secondary (V_B) components, respectively, as listed in the WDS. As a sanity test, the integrated apparent magnitude for the system V_t (from the WDS individual component photometry) is

⁸ Available at <https://www.usno.navy.mil/USNO/astrometry/optical-IR-prod/wds/orb6>.

⁹ Updated regularly and available at <https://sb9.astro.ulb.ac.be/>.

¹⁰ The latest version, called int4, is available at <https://www.usno.navy.mil/USNO/astrometry/optical-IR-prod/wds/int4/fourth-catalog-of-interferometric-measurements-of-binary-stars>.

Table 1
Object Identification and Basic Photometry

WDS Name HD Number	Discoverer Designation	HIP Number	V_{SIMBAD}^a	V_{Hip}^b	Source $_{V_{\text{Hip}}}^c$	$(V - I)_{\text{Hip}}^b$	Source $_{(V-I)_{\text{Hip}}}^d$	V_A^c	V_B^c	V_I	Δy^f	ΔI^f	Sp. Type WDS/SIMBAD
00352–0336 3196	HO212AB	2762	5.201 ± 0.009	5.2	G	0.64 ± 0.02	A	5.61	6.9	5.32	1.33 ± 0.06	1.17 ± 0.06	F8V/F7V+G4V
02128–0224 13612	TOK39Aa,Ab	10305	5.66 ± 0.01	5.65	H	0.63 ± 0	G	6.18	6.69	5.65	0.35 ± 0.40	...	F8V/F8V
04107–0452 26441	A2801	19508	7.35 ± 0.01	7.36	G	0.71 ± 0.00	H	8.3	8.3	7.55	0.80 ± 0.10	0.57 ± 0.28	G0/G3/5IV
04184+2135 27176	MCA14Aa,Ab	20087	5.631 ± 0.005	5.64	H	0.34 ± 0.03	C	5.6	8.1	5.50	F0V/F0V
07518–1354 64096	BU101	38382	...	5.16	G	0.67 ± 0.02	A	5.61	6.49	5.21	0.93 ± 0.16	0.83 ± 0.06	G1V/G0V
11560+3520 103613	CHR258	58184	6.74 ± 0.01	6.74	H	0.60 ± 0.01	L	7.0	9.1	6.85	F5/F5
14492+1013 130669	A2983	72479	...	8.42	H	0.91 ± 0.01	H	9.27	9.36	8.56	0.22 ± 0.26	0.43 ± 0.12	K2VK2V
15282–0921 137763	BAG25Aa,Ab	75718	6.883	6.89	G	0.86 ± 0.02	A	6.9	10.2	6.85	3.52 ± 0.19	2.28 ± 0.22	G9V/G9V
16584+3943 153527	COU1289	83064	8.09 ± 0.01	8.09	H	0.65 ± 0.01	H	8.4	8.4	7.65	G0/G0
18384–0312 172088	A88AB	91394	6.482 ± 0.010	6.49	G	0.64 ± 0.07	F	7.22	7.51	6.60	0.15 ± 0.20	0.0	F9V/F8V
20102+4357 191854	STT400	99376	...	7.41	H	0.73 ± 0.00	H	7.6	9.83	7.47	G3V/G4V+G8V
20205+4351 193793	IOT2Aa,Ab	100287	6.85	6.78	G	0.53 ± 0.00	H	6.85	WR+O/WC7p+O5
20527+4607 ...	A750	103055	8.709 ± 0.015	8.65	H	0.83 ± 0.01	L	9.11	10.26	8.79	G8V/G8V
23485+2539 223323	DSG8	117415	7.070 ± 0.009	7.08	H	0.51 ± 0.01	L	7.8	7.9	7.10	F5V+F5.5V/F2IV–V

Notes.^a From the SIMBAD database.^b From the Hipparcos mission, VizieR catalog I/239.^c G = ground-based, H = HIP.^d “A” for an observation of $V - I$ in the Cousins system; “F,” “G,” “H,” and “T” when $V - I$ was derived from measurements in other bands/photoelectric systems; “L” when $V - I$ was derived from Hipparcos and Star Mapper photometry.^e From the WDS.^f From our own HRCam@SOAR measurements in the Strömgren y or Cousins I band, respectively. When there is more than one measurement, it is the average. When there are more than three measurements, we quote the standard deviation on the mean.

Table 2
Additional Photometry from Recent All-sky Surveys

WDS Name HD Number	Discoverer Designation	V_{ASAS}	$V_{ASAS-SN}$	V_{APASS}	i'_{APASS}	V_{PD2010}	I_{PD2010}
00352–0336 3196	HO212AB	$5.772 \pm 0.306^{**}$	$5.69 \pm 0.644^{**}$	$6.157 \pm 0.078^*$	5.148 ± 0.012	5.203	4.58
02128–0224 13612	TOK39Aa,Ab	$6.046 \pm 0.194^{**}$...	$6.084 \pm 0.001^*$	5.482 ± 0.001	5.663	5.06
04107–0452 26441	A2801	$7.352 \pm 0.34^*$...	7.403 ± 0.04	7.214 ± 0.069	7.385	6.65
04184+2135 27176	MCA14Aa,Ab	$6.171 \pm 0.319^{**}$	$6.24 \pm 0.119^{**}$	5.625	5.29
07518–1354 64096	BU101	$5.91 \pm 0.244^{**}$...	$6.366 \pm 0.049^*$	5.333 ± 0.025	5.202	4.51
11560+3520 103613	CHR258	...	$6.24 \pm 0.119^{**}$	6.729	6.12
14492+1013 130669	A2983	8.401 ± 0.032	$8.96 \pm 0.109^{**}$	8.403 ± 0.058	7.772 ± 0.024	8.421	7.54
15282–0921 137763	BAG25Aa,Ab	$6.883 \pm 0.032^{**}$	11.39 ± 1.084^a	$6.939 \pm 0.111^*$...	6.864	5.99
16584+3943 153527	COU1289	...	$8.52 \pm 0.094^{**}$	8.093	7.4
18384–0312 172088	A88AB	$6.543 \pm 0.052^{**}$...	$6.862 \pm 0.01^*$...	6.484	5.81
20102+4357 191854	STT400	...	$7.92 \pm 0.097^{**}$	7.425	6.70
20205+4351 193793	IOT2Aa,Ab	...	$7.67 \pm 0.091^{**}$	6.757	6.03
20527+4607 ...	A750	...	$8.98 \pm 0.09^{**}$	8.677	7.82
23485+2539 223323	DSG8	$7.057 \pm 0.028^*$	$7.54 \pm 0.114^{**}$	7.042	6.52

Note.

^a 5'' away from the target, possible misidentification.

given in the 11th column.¹¹ In the 12th and 13th columns, we report our own measured magnitude differences in the Strömgren γ ($\Delta\gamma$) filter and Cousins I filter ΔI ($\equiv I_B - I_A$ between secondary and primary), respectively. These measurements are part of our speckle binary program mentioned in the previous paragraph. Finally, in the last column, we report the spectral type and luminosity class for the primary and secondary, after the plus sign, when available, from WDS and SIMBAD, respectively.

Precise photometry is required to place the individual components in an H-R diagram (Section 6). While there is an overall good agreement between SIMBAD, Hipparcos, and the combined (V_i) magnitudes, the quality of the photometry presented in Table 1 is somewhat variable, as can be readily seen by comparing the fourth, fifth, and 11th columns of that table. Therefore, in order to increase our comparison basis, we have searched for additional photometry of our targets in more recent all-sky photometric surveys for bright stars, in particular, the All Sky Automated Survey (ASAS;¹² Pojmanski 1997), the All-Sky Automated Survey for Supernovae (ASAS-SN;¹³ Kochanek et al. 2017; Jayasinghe et al. 2019), and the AAVSO Photometric All-Sky Survey (APASS;¹⁴ Henden et al. 2009, data release 2018 November 10). All three catalogs report V -band magnitudes. APASS includes Sloan i' -band photometry,

which unfortunately cannot be compared directly with I -band values from Hipparcos. To have an extra comparison source in the I bandpass, we used the all-sky spectrally matched Tycho-2 stars available at the CDS.¹⁵ This catalog presents synthetic photometry in various bands, including V and I , from a spectral energy distribution (SED) fit to 2.4 million stars in the Tycho-2 catalog by Pickles & Depagne (2010, hereafter PD2010). In Table 2, we present the photometry obtained from the above catalogs, together with their quoted uncertainties. While the above surveys measure and report everything they detect, their photometry is not reliable at the bright end. Based on the description of the different surveys, the reliability limit for ASAS, ASAS-SN, and APASS is 8, 10, and 7 mag, respectively. Therefore, in Table 2, we indicate dubious values (up to 1 mag brighter than the bright magnitude limit for each survey) with an asterisk and even brighter objects whose measurements should be considered very uncertain with a double asterisk. As can be seen from Table 2, since most of our targets are quite bright, the photometry from these surveys is unfortunately not very reliable for some of them. An important point to make here is that while many of our targets do have high-quality Gaia photometry, it is unfortunately not useful for our purposes due to the special bandpass adopted by the mission (Maíz Apellániz 2017),¹⁶ which does not agree with

¹¹ Computed as $V_i = -2.5 \times \log(10^{-0.4V_A} + 10^{-0.4V_B})$.

¹² <http://www.astro.uw.edu/pl/asas/?page=main>

¹³ <http://www.astronomy.ohio-state.edu/asassn/index.shtml>

¹⁴ <https://www.aavso.org/apass>

¹⁵ VizieR catalog VI/135.

¹⁶ See also <https://www.cosmos.esa.int/web/gaia/edr3-passbands> and Riello et al. (2021).

the bandpass in which we measure magnitude differences at SOAR or the passbands used in the WDS.

In Figure 1, we show a comparison of the V and I photometry presented in Tables 1 and 2. We chose to plot Hipparcos magnitudes in the abscissa because they are the largest and most homogeneous data set for our sample of targets. As can be seen in this figure, there is a relatively good correspondence in the V band between the photometry from Hipparcos and that from SIMBAD and also with the combined photometry V_t from WDS. The fit of V_{SIMBAD} versus V_{Hip} has an rms residual of 0.053 mag, while that of V_t versus V_{Hip} is 0.17 mag. The larger rms for the latter can be explained mostly by one measurement: the V_t for COU1289 is too bright in comparison with V_{Hip} (which is the value adopted by SIMBAD too; see Table 1). This object is further discussed in Section 5. Based on our photometric comparisons, we will thus adopt 0.06 mag as an estimate of the uncertainty of the photometry in Section 4; see also Figures 5 and 6.

As can be seen in Figure 1, at the bright end ($V < 7.0$), the ASAS and APASS magnitudes exhibit larger photometric errors and scatter, consistent with their declared bright-end reliability. In the case of ASAS-SN, this problem extends down to the faintest data plotted with ASAS photometry ($V \sim 9$). The ASAS-SN V for object BAG25Aa,Ab is an extreme outlier, but we believe this is due to a misidentification of another object near the target located at a distance of $5''$, because the binary is too bright for the survey (in contrast, the available measurements from the other surveys cluster around the one-to-one relationship). In the range $V > 7.0$, both ASAS and APASS exhibit good consistency within the errors, between each other, and with Hipparcos and SIMBAD.

For the I band, the comparison is restricted only to the PD2010 SED-fitted photometry and the Sloan i' filter measurements from the APASS survey. As shown in Mendez et al. (2021), there is an offset of about 0.38 mag between APASS i' and I , which is depicted by the dotted-dashed line in the plot. After applying this offset, the APASS i' -band photometry is commensurable to that derived by Hipparcos and PD2010. In general, we appreciate a good correspondence between Hipparcos, PD2010, and APASS, with an overall rms of the one-to-one fit of 0.06 mag, i.e., similar to the one found for the V band.

2.1. Individual Component Magnitudes

To place our targets in an H-R diagram (see Section 4), individual component magnitudes are needed. The I -band combined magnitude for each system was computed from $I_{\text{Hip}} = V_{\text{Hip}} - (V - I)_{\text{Hip}}$, and the individual I component magnitudes are as follows: $I_A = I_{\text{Hip}} + 2.5 \times \log(1.0 + 10^{-0.4\Delta I})$ (primary) and $I_B = I_A + \Delta I$ (secondary). For the V band, we used either the Hipparcos system magnitudes and the WDS magnitude differences or our own value ΔV derived from our measured values of Δy quoted in Table 1, depending on the location of the binary on the H-R diagram relative to the theoretical isochrones plotted (see Section 4).

From the data in Table 1, it can be seen that the Hipparcos photometry is generally in good agreement with the photometry for the system given in WDS (V_t) and SIMBAD, as well as that from other photometric surveys (see Table 2). Furthermore, if we define $\Delta V = V_B - V_A$, the mean difference $\langle \Delta V - \Delta y \rangle = -0.13 \pm 0.32$ mag for seven objects in Table 1 is in agreement with Tokovinin et al. (2010) and Mendez et al. (2021),

indicating that our SOAR magnitude differences seem reliable. This gives us some confidence on the photometry presented, but see the extended discussion about this for individual objects in Section 5 and Figures 5 and 6 in Section 4.

For one target, IOT2Aa,Ab, individual component magnitudes are not available in WDS, and, being a northern target, it was not observed at SOAR. Several other, mostly northern, targets in Table 1 also lack a measured ΔI ; hence, we could not compute individual component magnitudes for them.

3. Orbital Elements, Orbital Parallaxes, and Individual Component Mass

As mentioned in Section 2, the astrometric data used in this work are a combination of published information from WDS with recent measurements made with the HRCam speckle camera¹⁷ mounted on the SOAR 4.1 m telescope in the context of the program described in Mendez et al. (2017). Part of our data has not been published yet.¹⁸

Regarding the uncertainty or equivalent weight of the historical data that we included in our orbit calculations, we adopted the value indicated in the WDS, when available, or errors typical for the observational procedure used (e.g., interferometric/digital imaging/photographic/micrometer). On the other hand, HRCam has been shown to deliver a precision of 1–3 mas in angular separation for objects brighter than $V \sim 12$ on a routine basis (Tokovinin 2018). In our HRCam@SOAR survey, “calibration binaries,” binaries with very well-known orbits (grades 1 or 2 in Orb6), are observed every night to calibrate our measurements, leading to systematic errors of less than 0.1° in position angle and better than 0.2% in scale, smaller than our internal precision.¹⁹ The exact final precision of our measurements depends, however, on a number of factors, but in this paper, we will adopt an uncertainty of 3 mas as representative of all of our HRCam data. As emphasized in Mendez et al. (2017), one should bear in mind that the assignment of weights to each observational point is somewhat subjective (especially for older data) and plays an important role in the orbital solution. Slightly different orbital solutions from authors using the same astrometric data set are in some cases due to different weighting.

Orbits have been derived using our Markov Chain Monte Carlo (MCMC) code. In order to reduce the dimensions of the search space, we adopt the parameterization of Mendez et al. (2017), in which elements P , T , e , Ω , i , mass ratio $q = m_B/m_A$, and parallax ϖ are explored via MCMC, whereas a (semimajor axis), ω , and V_{CoM} are calculated analytically via the exact least-squares solution given (P , T , e , Ω , i , q , ϖ). The details can be found in Mendez et al. (2017), where an MCMC algorithm is used to carry out joint estimation of orbital parameters and RV (see Mendez et al. 2017, Appendix A, for details of the least-squares estimate).

From a methodological standpoint, the only difference between the algorithm utilized here and that of Mendez et al. (2017) is that in the present work, we lift the restriction

¹⁷ For up-to-date details of the instrument, see <http://www.ctio.noao.edu/~atokovin/speckle/>.

¹⁸ At the site http://www.das.uchile.cl/~rmendez/B_Research/JAA-RAM-SB2/, we make available our input files, indicating the adopted uncertainty and quadrant flips, if any, for each data entry and the origin of the measurements in the last column, following the nomenclature in int4.

¹⁹ One of these “astrometric standards,” WDS 07518–1354 = BU101, is an SB2 and included in this paper; see Section 5.

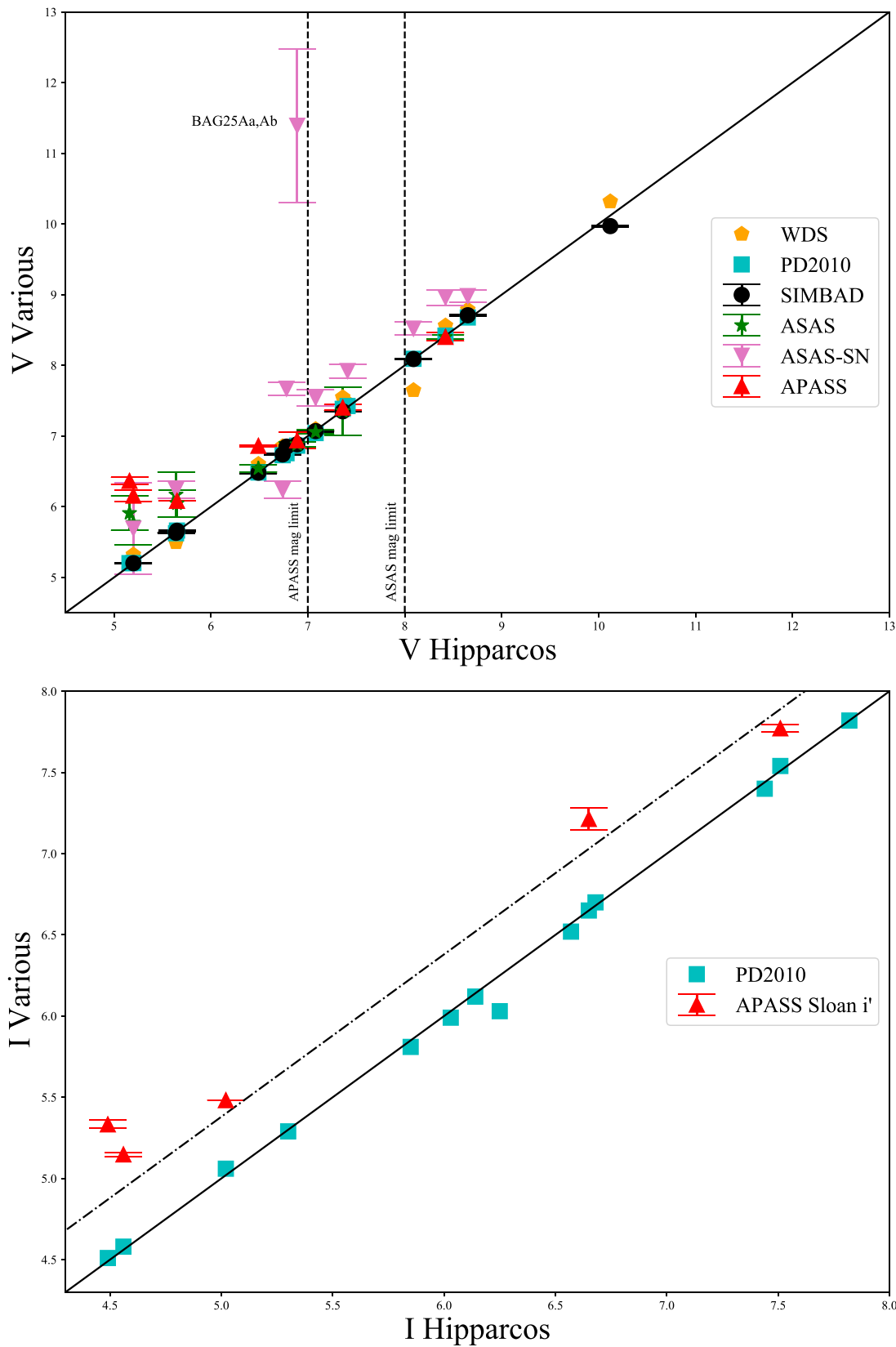


Figure 1. Comparison of Hipparcos V - (top panel) and I -band magnitudes (bottom panel) with other photometric data presented in Tables 1 and 2. The dotted vertical lines in the top panel show the reliably bright limits of the APASS ($V = 7$) and ASAS ($V = 8$) surveys. In the whole magnitude range covered by these figures, all ASAS-SN photometry is unreliable (note the large declared error bars), but it was included for completeness. In both panels, the diagonal solid line depicts a one-to-one relationship. In the bottom panel, the diagonal dotted-dashed line shows the 0.38 mag offset between I and i' from APASS found by Mendez et al. (2021, their Figure 1). The highly discrepant point for Bag25Aa,Ab from ASAS-SN in the top panel is probably due to a misidentification of the target. See text for details.

$q = m_B/m_A < 1$. This allows the algorithm to handle uncertainty about the primary and secondary stars; if the mass ratio q is greater than 1, the algorithm simply calculates the parameters as if m_B was the primary (this “swap” leaves all parameters other than ω and Ω untouched). While the value m_B/m_A (i.e., q) reported in Table 4 is just a natural element of the parameterization adopted (and hence a raw output of the MCMC algorithm), amplitudes K_A and K_B in Table 3 are calculated as a function of the values of P , e , q , a , $\sin i$, and ϖ of each MCMC sample.

Since the code incorporates the parallax of the system as an unknown parameter of the estimation process, it allows us to determine dynamically self-consistent orbital parallaxes, as originally suggested by Pourbaix (2000). Additionally, SB2s allow a calculation of individual component masses because the astrometric solution gives the mass sum, while the amplitudes of the RV curve give the mass ratio. Our code produces posterior probability distribution functions (PDFs) for all of the physical and geometrical parameters involved. These PDFs allow us to reliably estimate parameter uncertainties in the following way. It is customary to represent the uncertainties in terms of the dispersion σ , but this quantity is well defined only for orbits where the PDFs are “well behaved” (e.g., they are symmetrical), and it becomes meaningless for orbits that may exhibit long tails, as in the case of uncertain orbits. For this reason, we instead adopt the upper (third) quartile (Q75) and lower (first) quartile (Q25) of the distribution as a measure of the spread of the corresponding PDF and hence as a quantitative measure of the dispersion (uncertainty) of the corresponding parameter,²⁰ which is consistent with the available data and the underlying Keplerian model.

We ran our MCMC routine with a chain length of 2 million samples and a burn-in period of 50,000 iterations. The comparatively short burn-in time is explained on the grounds that the target parameters were initialized favorably; we fed the MCMC routine with approximate initial values from the optimization-based routine ORBIT developed by Tokovinin (1992).²¹ From the steadiness of the average value of the orbital parameters over time, we conclude that all of the solutions obtained are stable. It is worth noting that an added benefit of the large number of samples generated is that the resulting PDF histograms look rather smooth (see Figures 3 and 8), despite the fact that they are based directly on the MCMC samples; i.e., they are raw histograms rather than kernel-smoothed densities as in, e.g., Wand & Jones (1994).

The results from our MCMC code for the 14 SB2s selected as explained in Section 2 are given in Table 3. In the first two columns, we give the WDS name and the source of the previous orbital information, if available. In the following columns, we present the seven classical orbital elements, the RV for the center of mass of the system (V_{CoM}), and the semiamplitudes for the primary (K_1) and secondary (K_2). In the penultimate column, we indicate the grade of the orbit according to Orb6 (1: best, 5: worst) and SB9 (5: best, 1: worst), and in the last column, we give the reference to the most recently published astrometric orbit (from Orb6) or RV solution (from SB9). For each object in this table, two sets of values for the orbital elements are provided. The upper

row gives the maximum-likelihood (ML) value. For an explanation of why this is the selected estimator, please see the discussion in Mendez et al. (2021, Section 3.1). The lower row gives the median derived from the posterior PDF of the MCMC simulations, as well as the upper (Q75) and lower (Q25) quartile of the distribution in the form of a superscript and subscript, respectively. As explained before, the quartiles give us an estimation of the uncertainty of our estimated parameters. A look at the results in this table indicates that our values generally coincide quite well with those from previous studies. In particular, it is well known that the argument of periastris (ω) is well determined by RV measurements as long as the distinction between primary and secondary is unambiguous (difficult, e.g., for equal-mass binaries); the table shows that our values are indeed quite close to those from SB9, albeit with smaller uncertainties in our case. On the other hand, the longitude of the ascending node (Ω) can be well determined from astrometric observations alone, but it suffers from the same ambiguity in the case of equal-brightness binaries. From the table, we see that there is good correspondence between our values for Ω and those from Orb6 (but again, with smaller formal uncertainties in our case), except for five objects. As will be shown below, four of these objects have values of the mass ratio q quite close to 1, which probably explains this discrepancy.

In Figure 2, we show a subset of representative examples of orbital solutions from our simultaneous fit to the astrometric orbit (left panels) and the RV curve (right panels), and in Figure 3, we present the PDFs for the same three systems. Inspection of Table 3 and Figures 2 and 3 shows that well-determined orbits have an ML value that approximately coincides with the second quartile of the PDF, their interquartile range is relatively well constrained, and the PDFs have a Gaussian-like distribution. On the contrary, poor orbits show PDFs with long tails—and therefore large interquartile ranges—on which the ML value usually differs significantly from the second quartile, and the PDFs are tangled. The top panel of Figure 8 shows an extreme case in this respect: TOK39Aa,Ab. For completeness, in http://www.das.uchile.cl/~rmendez/B_Research/JAA-RAM-SB2/, we make available the orbital plots and relevant PDFs for all of the systems in our sample. Even though the astrometric orbits do not always have excellent phase coverage, the combined solution produces very precise orbital parameters. This is most evident in Figure 3, which exhibits tight and well-constrained distributions. Judging from our quartile-based uncertainty estimation, we can see that the mass ratio for this sample of objects is determined in the best cases with less than 1% error, while the uncertainty on the mass sum is around 1%. The formal error on the best individual component masses that we could determine is $0.01 M_\odot$ (see Table 4).

In Table 4, we present a comparison of the parallax values from Hipparcos and/or Gaia eDR3 with our orbital parallaxes. In the last four columns, we give the mass ratio, the total mass, and the individual masses obtained from our simultaneous fits to the astrometric and RV data, which was done adopting the orbital elements given in Table 3. The first line gives the ML values, and the second line gives the quartiles. All mass values were computed allowing the parallax of the system to be a free parameter of the MCMC code, i.e., using the orbital parallax,²²

²⁰ For a Gaussian function, one can convert from one to the other using the fact that $\sigma = (Q75 - Q25)/1.349$.

²¹ The code and user manual can be downloaded from <http://www.ctio.noao.edu/~atokovin/orbit/index.html>. We note that this code fits the RV amplitudes independently from the visual orbits, and hence it does not directly compute an orbital parallax. For this reason, ORBIT was used only to obtain preliminary orbital parameters to initialize our MCMC code.

²² Except for target TOK39Aa,Ab = WDS 02128–0224, for which we used a parallax prior; see Section 5 and Figure 8. In fact, in Table 4, we report both solutions for this target: with and without a parallax prior.

Table 3
Extended Orbital Elements for our SB2s

WDS Name HD Number	Source	P (yr)	T_0 (yr)	e	a (mas)	ω (deg)	Ω (deg)	i (deg)	V_{CoM} (km s $^{-1}$)	K_1 (km s $^{-1}$)	K_2 (km s $^{-1}$)	Gr	Orbit Author
00352–0336	This paper	6.8975	1890.6130	0.7616	234.26	104.73	328.34	47.89	9.09	11.67	15.64		
3196	ORB6 SB9	6.8975 $^{+0.0005}_{-0.0006}$ 6.89 6.9185-Fixed	1890.6139 $^{+0.0091}_{-0.0085}$ 2000.98 1987.187 \pm 0.011	0.7615 $^{+0.0013}_{-0.0014}$ 0.773 0.77-Fixed	234.07 $^{+0.74}_{-0.73}$ 241 ...	104.70 $^{+0.18}_{-0.18}$ 283.8 109.0 \pm 3.1	328.39 $^{+0.22}_{-0.22}$ 149.0 ...	47.83 $^{+0.24}_{-0.24}$ 49.4 ...	9.08 $^{+0.03}_{-0.03}$... 8.83 \pm 0.22	11.68 $^{+0.51}_{-0.51}$... 10.90 \pm 0.59	15.59 $^{+0.17}_{-0.17}$... 16.44 \pm 0.43	1	Mason et al. (2005) Duquennoy & Mayor (1991)
02128–0224	This paper	0.259516	1983.85112	0.6917	13.82	76.28	240.2	23.9	–5.95	19.01	19.65		
13612	ORB6 SB9	0.259516 $^{+0.000011}_{-0.000011}$...	1983.85112 $^{+0.00027}_{-0.00026}$...	0.6920 $^{+0.0027}_{-0.0027}$...	13.98 $^{+0.75}_{-0.64}$...	76.23 $^{+0.41}_{-0.41}$...	240.3 $^{+1.4}_{-1.3}$...	25.6 $^{+6.4}_{-7.8}$...	–5.95 $^{+0.02}_{-0.02}$...	19.01 $^{+0.04}_{-0.04}$...	19.74 $^{+0.40}_{-0.43}$
04107–0452	This paper	0.259515 \pm 0.000012 20.6327	1989.55859 \pm 0.00015 1931.498	0.689 \pm 0.003 0.8349	164.32 164.32	74.3 \pm 0.5 67.88	–5.95 \pm 0.07 26.49	19.08 \pm 0.15 11.65	19.77 \pm 0.15 12.41	...	Duquennoy & Mayor (1991)
26441	ORB6 SB9	20.6290 $^{+0.0077}_{-0.0076}$ 20.621 \pm 0.005 20.608 \pm 0.011	1931.513 $^{+0.031}_{-0.031}$ 2014.031 \pm 0.003 1993.426 \pm 0.011	0.8384 $^{+0.0011}_{-0.0011}$ 0.8400 \pm 0.0014 0.8372 \pm 0.0015	164.72 $^{+0.66}_{-0.66}$ 167.2 \pm 2.1 ...	67.94 $^{+0.18}_{-0.18}$ 68.6 \pm 0.3 69.0 \pm 0.4	154.20 $^{+0.28}_{-0.28}$ 153.3 \pm 0.6 ...	67.81 $^{+0.23}_{-0.24}$ 69.0 \pm 0.5 ...	26.49 $^{+0.00}_{-0.00}$... 26.55 \pm 0.03	11.61 $^{+0.04}_{-0.04}$... 11.59 \pm 0.06	12.41 $^{+0.06}_{-0.06}$... 12.51 \pm 0.10	2 5	Tokovinin (2017) Griffin (2015)
04184+2135	This paper	11.3630	1955.100	0.1537	135.39	162.61	352.25	123.88	37.79	7.46	8.97		
27176	ORB6 SB9	11.3642 $^{+0.0071}_{-0.0071}$ 11.350 \pm 0.021 11.323 \pm 0.016	1955.100 $^{+0.031}_{-0.030}$ 1977.740 \pm 0.056 1989.075 \pm 0.038	0.1540 $^{+0.0016}_{-0.0016}$ 0.1670 \pm 0.0044 0.1711 \pm 0.0028	135.37 $^{+0.16}_{-0.16}$ 132.90 \pm 0.95 ...	162.67 $^{+0.80}_{-0.80}$ 339. \pm 1.9 159.1 \pm 1.3	352.22 $^{+0.24}_{-0.24}$ 350.70 \pm 0.61 ...	123.88 $^{+0.25}_{-0.25}$ 125.50 \pm 0.73 ...	37.79 $^{+0.01}_{-0.01}$... 37.78 \pm 0.12	7.50 $^{+0.32}_{-0.32}$... 7.32 \pm 0.48	8.96 $^{+0.11}_{-0.11}$... 9.01 \pm 0.16	2 ...	Pourbaix (2000) Torres et al. (1997)
07518–1354	This paper	23.3225	1892.630	0.7537	611.9	253.174	103.054	80.839	–21.37	9.76	9.75		
64096	ORB6 SB9	23.3207 $^{+0.0054}_{-0.0053}$ 23.330 \pm 0.010 22.701 \pm 0.027	1892.639 $^{+0.026}_{-0.027}$ 1985.923 \pm 0.011 1985.914 \pm 0.020	0.7538 $^{+0.0015}_{-0.0015}$ 0.7647 \pm 0.0021 0.741 \pm 0.007	612.0 $^{+1.7}_{-1.6}$ 617.9 \pm 2.4 ...	253.185 $^{+0.080}_{-0.079}$ 253.64 \pm 0.12 253.1 \pm 0.4	103.044 $^{+0.059}_{-0.061}$ 282.65 \pm 0.09 ...	80.835 $^{+0.045}_{-0.044}$ 80.82 \pm 0.06 ...	–21.38 $^{+0.02}_{-0.02}$... –21.34 \pm 0.16	9.70 $^{+0.15}_{-0.15}$... 9.13 \pm 0.63	9.69 $^{+0.47}_{-0.46}$... 9.69 \pm 0.26	1 5	Tokovinin (2012) Pourbaix (2000)
11560+3520	This paper	13.553	1996.16	0.1010	127.7	316.3	279.5	145.4	–4.99	4.19	4.99		
103613	ORB6 SB9	13.566 $^{+0.057}_{-0.056}$ 13.53 13.66 \pm 0.15	1996.11 $^{+0.18}_{-0.19}$ 2010.54 2009.46 \pm 0.30	0.1008 $^{+0.0054}_{-0.0054}$ 0.165 0.103 \pm 0.011	127.6 $^{+2.0}_{-2.0}$ 143 ...	315.3 $^{+4.0}_{-4.0}$ 9.90 309 \pm 8	279.9 $^{+1.3}_{-1.3}$ 302.5 ...	146.1 $^{+3.7}_{-3.3}$ 135.1 ...	–4.99 $^{+0.01}_{-0.01}$... –4.97 \pm 0.04	4.19 $^{+0.12}_{-0.12}$... 5.00 \pm 0.06	4.98 $^{+0.02}_{-0.02}$... 4.25 \pm 0.16	3 5	Griffin & Mason (2013) Griffin (2013a)
14492+1013	This paper	10.0052	1988.130	0.4994	125.174	162.22	319.48	44.44	–88.29	6.66	6.61		
130669	ORB6 SB9	10.0062 $^{+0.0041}_{-0.0042}$ 10.010 9.91 \pm 0.18	1988.130 $^{+0.014}_{-0.014}$ 2018.174 2008.127 \pm 0.030	0.4999 $^{+0.0022}_{-0.0021}$ 0.518 0.488 \pm 0.009	125.07 $^{+0.35}_{-0.35}$ 123 ...	162.31 $^{+0.67}_{-0.68}$ 335.9 163.0 \pm 2.0	319.43 $^{+0.47}_{-0.47}$ 144.8 ...	44.30 $^{+0.48}_{-0.48}$ 43.5 ...	–88.29 $^{+0.01}_{-0.01}$... –88.27 \pm 0.05	6.65 $^{+0.06}_{-0.06}$... 6.73 \pm 0.07	6.61 $^{+0.09}_{-0.10}$... 6.76 \pm 0.09	1 5	Docobo et al. (2018a) Griffin (2015)
15282–0921	This paper	2.4359	1980.4630	0.97525	104.3	254.898	272.47	54.3	7.16	37.45	55.65		
137763	ORB6 SB9	2.4359 $^{+0.0001}_{-0.0001}$ 2.43623 2.436175 \pm 0.000047	1980.4629 $^{+0.0002}_{-0.0002}$ 2007.2603 1990.205532 \pm 0.000041	0.97530 $^{+0.00011}_{-0.00011}$ 0.976 0.9733 \pm 0.0006	104.7 $^{+2.4}_{-2.4}$ 107.4 \pm 8.1 ...	254.888 $^{+0.058}_{-0.059}$ 255.6 252.64 \pm 0.73	272.64 $^{+0.64}_{-0.64}$ 272.8 \pm 2.1 ...	54.5 $^{+1.1}_{-1.2}$ 55.4 \pm 3.6 ...	7.16 $^{+0.01}_{-0.01}$... 7.47 \pm 0.20	37.47 $^{+0.06}_{-0.06}$... 36.42 \pm 0.38	55.56 $^{+0.63}_{-0.63}$... 52.90 \pm 1.73	2 ...	Tokovinin (2016) Halbwachs et al. (2018)
16584+3943	This paper	16.023	1985.170	0.7732	75.40	336.04	245.46	109.38	33.54	10.46	11.90		
153527	ORB6 SB9	16.022 $^{+0.039}_{-0.039}$ 16.09 16.153-Fixed	1985.171 $^{+0.040}_{-0.040}$ 2001.07 2001.1970 \pm 0.0080	0.7729 $^{+0.0019}_{-0.0019}$ 0.753 0.775 \pm 0.003	75.38 $^{+0.41}_{-0.42}$ 75 ...	336.06 $^{+0.43}_{-0.43}$ 154.3 337.0 \pm 0.9	245.36 $^{+0.47}_{-0.46}$ 63.2 ...	109.55 $^{+0.83}_{-0.82}$ 113.0 ...	33.54 $^{+0.08}_{-0.08}$... 33.59 \pm 0.16	10.45 $^{+0.09}_{-0.09}$... 10.40 \pm 0.18	11.89 $^{+0.13}_{-0.13}$... 11.96 \pm 0.23	2 5	Docobo & Ling (2013) Griffin (2003)
18384–0312	This paper	12.1422	1910.000	0.2454	145.35	257.88	352.99	123.90	–15.97	7.21	7.55		
172088	ORB6 SB9	12.1426 $^{+0.0044}_{-0.0044}$ 12.135 \pm 0.006 12.1342-Fixed	1909.996 $^{+0.039}_{-0.039}$ 2007.18 \pm 0.04 2007.185 \pm 0.049	0.2456 $^{+0.0019}_{-0.0019}$ 0.2567 \pm 0.0029 0.230 \pm 0.006	145.37 $^{+0.38}_{-0.39}$ 146.1 \pm 0.8 ...	257.87 $^{+0.30}_{-0.30}$ 79.7 \pm 1.5 258.9 \pm 1.5	353.03 $^{+0.22}_{-0.22}$ 173.4 \pm 0.9 ...	123.87 $^{+0.22}_{-0.22}$ 123.9 \pm 5.0 ...	–15.97 $^{+0.00}_{-0.00}$... –15.95 \pm 0.03	7.20 $^{+0.03}_{-0.03}$... 7.19 \pm 0.06	7.55 $^{+0.03}_{-0.03}$... 7.51 \pm 0.06	1 5	Griffin (2013b) Griffin (2013b)

Table 3
(Continued)

WDS Name HD Number	Source	P (yr)	T_0 (yr)	e	a (mas)	ω (deg)	Ω (deg)	i (deg)	V_{CoM} (km s $^{-1}$)	K_1 (km s $^{-1}$)	K_2 (km s $^{-1}$)	Gr	Orbit Author
20102+4357	This paper	85.05	1886.15	0.4945	448.6	344.00	143.75	117.15	-42.99	3.51	5.40		
191854		85.02 $^{+0.27}_{-0.27}$	1886.22 $^{+0.27}_{-0.28}$	0.4889 $^{+0.0035}_{-0.0035}$	448.2 $^{+1.34}_{-1.3}$	344.07 $^{+0.82}_{-0.82}$	143.75 $^{+0.25}_{-0.26}$	117.22 $^{+0.28}_{-0.28}$	-43.06 $^{+0.13}_{-0.14}$	3.65 $^{+0.37}_{-0.36}$	5.07 $^{+0.47}_{-0.49}$	2	Heintz (1997)
	ORB6	85.61	1970.27	0.488	449	339.4	142.2	116.4	
	SB9	85.22 \pm 0.12	1970.44 \pm 0.18	0.4922 \pm 0.0033	...	339 \pm 1	-43.2 \pm 0.2	3.97 \pm 0.44	5.12 \pm 0.47	...	Pourbaix (2000)
20205+4351	This paper	7.9232	1993.1840	0.9060	8.44	42.76	347.7	117.5	1.43	28.0	68.1		
193793		7.9241 $^{+0.0037}_{-0.0035}$	1993.1825 $^{+0.0036}_{-0.0039}$	0.9012 $^{+0.0034}_{-0.0034}$	8.30 $^{+0.22}_{-0.23}$	42.31 $^{+0.70}_{-0.68}$	349.1 $^{+2.5}_{-2.5}$	119.4 $^{+3.7}_{-3.4}$	1.25 $^{+0.05}_{-0.05}$	28.3 $^{+1.8}_{-1.8}$	68.5 $^{+1.2}_{-1.1}$	3	Monnier et al. (2011)
	ORB6	7.9298 \pm 0.0025	1985.2443 \pm 0.0082	0.901 \pm 0.005	8.99 \pm 0.19	48.2 \pm 1.9	354.2 \pm 0.7	118.9 \pm 0.9	Marchenko et al. (2003)
	SB9	7.9370 \pm 0.0036	1985.2225 \pm 0.0044	0.881 \pm 0.005	...	46.7 \pm 1.6	3.1 \pm 1.0	30.5 \pm 1.9	82.0 \pm 2.3	...	
20527+4607	This paper	31.141	1918.97	0.7505	236.7	321.90	47.72	127.52	-20.30	6.95	7.54		
...		31.144 $^{+0.052}_{-0.051}$	1918.97 $^{+0.10}_{-0.11}$	0.7510 $^{+0.0034}_{-0.0034}$	236.4 $^{+2.0}_{-2.0}$	322.01 $^{+0.67}_{-0.66}$	47.74 $^{+0.53}_{-0.54}$	127.57 $^{+0.89}_{-0.86}$	-20.31 $^{+0.04}_{-0.04}$	6.96 $^{+0.10}_{-0.10}$	7.54 $^{+0.10}_{-0.10}$	3	Docobo & Campo (2013)
	ORB6	30.45	2013.49	0.723	212	351.6	65.9	128.7	
	SB9	31.4853	1981.2329	0.74	...	320.	-20.3	6.9	7.5	2	Griffin (1984)
23485+2539	This paper	3.2163	2001.3988	0.6061	40.3	77.75	121.8	86.1	-9.55	16.43	16.35		
223323		3.2157 $^{+0.0035}_{-0.0035}$	2001.3995 $^{+0.0041}_{-0.0042}$	0.6060 $^{+0.0038}_{-0.0038}$	40.3 $^{+1.2}_{-1.2}$	77.79 $^{+0.60}_{-0.60}$	121.2 $^{+1.7}_{-1.7}$	86.0 $^{+1.3}_{-1.3}$	-9.55 $^{+0.01}_{-0.01}$	16.43 $^{+0.12}_{-0.12}$	16.35 $^{+0.12}_{-0.12}$	3	Horch et al. (2019b)
	ORB6	3.2191 \pm 0.0038	2011.0545 \pm 0.0085	0.602 \pm 0.008	40.8 \pm 1.0	78.4 \pm 0.6	121.1 \pm 1.1	86.0 \pm 0.9	
	SB9	3.2172 \pm 0.0036	2004.6134 \pm 0.0025	0.604 \pm 0.003	...	77.8 \pm 0.6	-9.56 \pm 0.06	16.38 \pm 0.11	16.40 \pm 0.16	...	Griffin (2007)

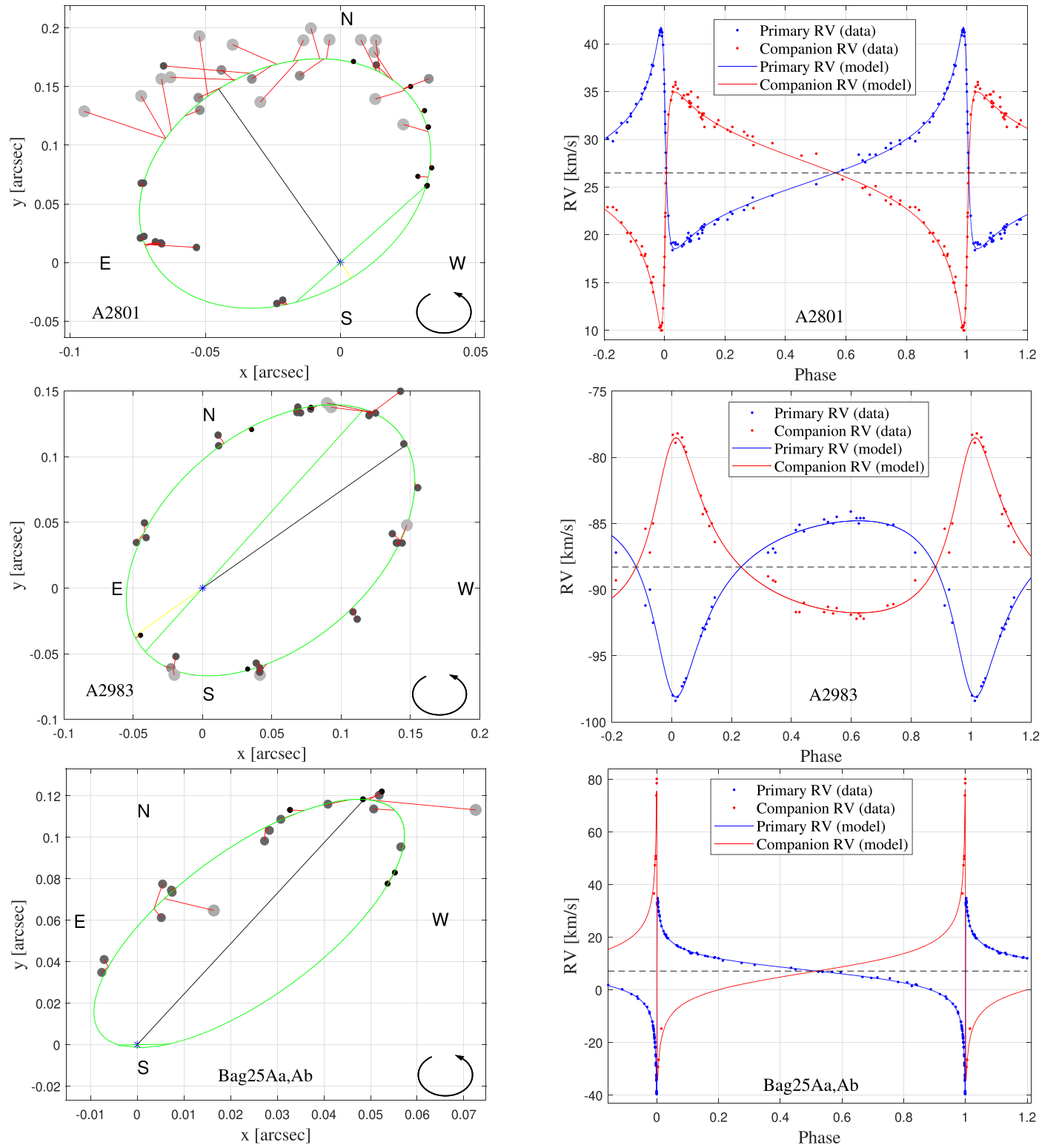


Figure 2. The ML orbits from simultaneous fits to the astrometric and RV curves for three representative cases. From top to bottom: A2801 (WDS 04107–0452), A2983 (WDS 14492+1013), and Bag25Aa,Ab (WDS 15282–0921). The left panels show the data points and astrometric orbit. The size and color of the dots indicate the weight (uncertainty) of each observation; large, light dots indicate larger errors, and the opposite is true for small, dark dots. Smaller dots are from more recent interferometric measurements, including—but not limited to—our own. The green line indicates the line of nodes, while the black line indicates the direction to apoastron. The right panels show the RV curves of both components. The horizontal dashed line indicates the inferred (fitted) systemic velocity reported in Table 3.

whose ML value and quartiles are given in the fourth column of this table (upper and lower row, respectively). Therefore, our mass estimates do include the extra variance from this parameter.

In Figure 4, we show a comparison of our orbital parallaxes with those from Hipparcos, Gaia, and the recent study of SB2s by Piccotti et al. (2020). The mean values of the differences $\langle \Pi_{\text{orb}} - \Pi_{\text{various}} \rangle$ are 0.0 ± 1.8 mas ($N = 13$ objects),

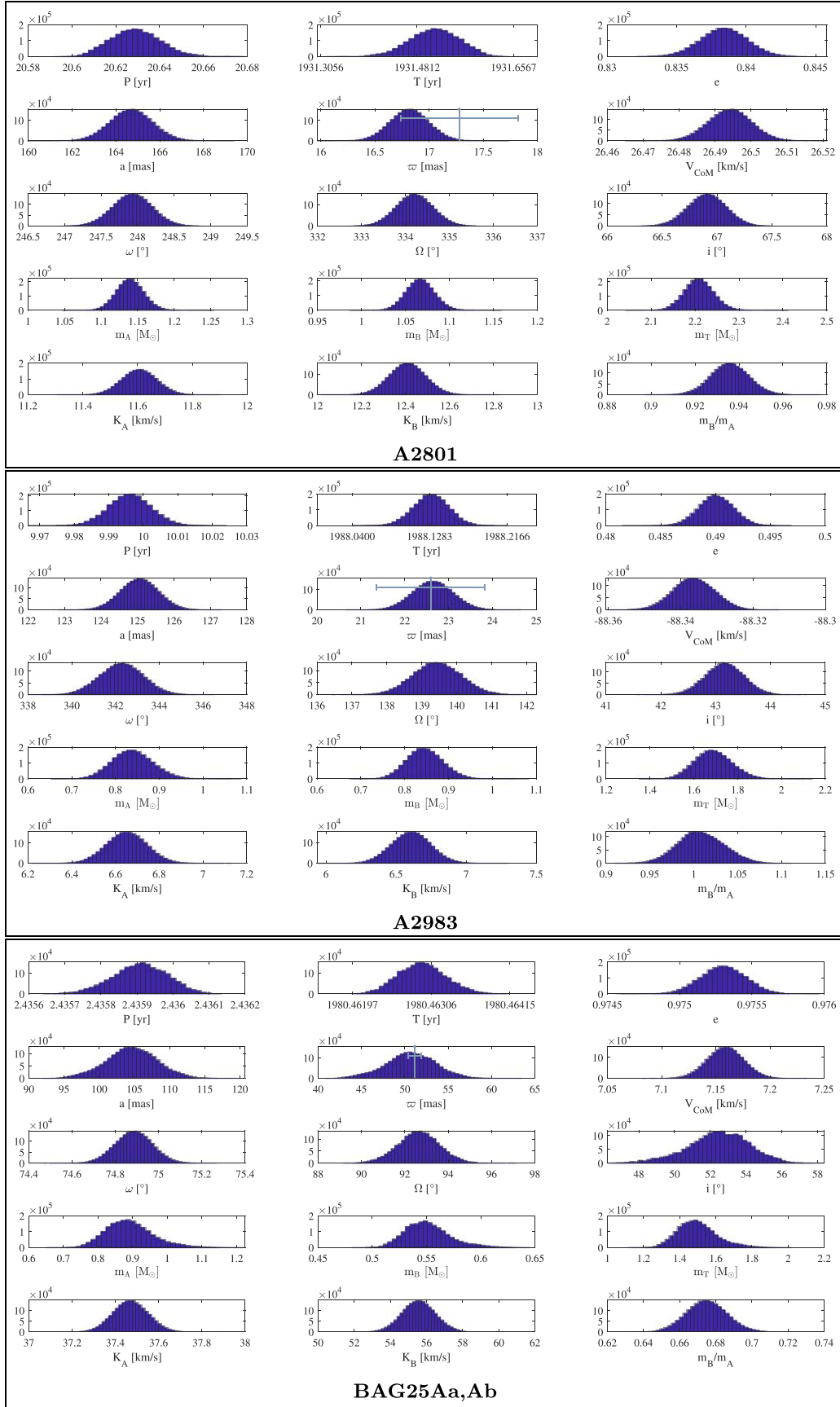


Figure 3. Posterior distributions of the seven classical orbital elements plus the (fitted) orbital parallax, the Gaia DR2 trigonometric parallax and its $\pm 1\sigma$ error, the systemic velocity, the velocity amplitudes for both components, the mass sum, the mass ratio, and the individual component masses for the same objects shown in Figure 2. We note that for objects with a mass ratio close to 1 (in this case, A2983, middle panel; but see Table 4 for other objects), the m_B/m_A histograms are well behaved and smooth across that boundary, as explained in the text.

Table 4
Parallaxes and Individual Component Masses

WDS Name HD Number	Hipparcos (mas)	Gaia eDR3 (mas)	Orbital (mas)	m_B/m_A	m_T M_\odot	m_A M_\odot	m_B M_\odot
00352–0336 3196	47.05 ± 0.67	...	42.41	0.746	3.54	2.03	1.51
02128–0224 ^a 13612	25.19 ± 1.41	26.54 ± 0.13	23.1 $24.8^{+7.2}_{-8.1}$	0.968 $0.963^{+0.022}_{-0.020}$	$3.54^{+0.21}_{-0.21}$ 3.2	$2.02^{+0.09}_{-0.09}$ 1.62	$1.52^{+0.13}_{-0.12}$ 1.57
02128–0224+prior ^a 13612	25.19 ± 1.41	26.54 ± 0.13	26.03 $26.29^{+0.21}_{-0.21}$	0.959 $0.960^{+0.022}_{-0.020}$	2.355 $2.301^{+0.087}_{-0.084}$	1.20 $1.17^{+0.05}_{-0.05}$	1.15 $1.13^{+0.04}_{-0.04}$
04107–0452 26441	16.09 ± 0.65	17.28 ± 0.54	16.58 $16.82^{+0.12}_{-0.12}$	0.9386 $0.9355^{+0.0059}_{-0.0058}$	2.286 $2.207^{+0.023}_{-0.022}$	1.18 $1.14^{+0.01}_{-0.01}$	1.11 $1.07^{+0.01}_{-0.01}$
04184+2135 27176	18.5 ± 0.5	19.51 ± 0.24	18.15 $18.11^{+0.39}_{-0.37}$	0.832 $0.837^{+0.037}_{-0.038}$	3.21 $3.23^{+0.20}_{-0.20}$	1.76 $1.76^{+0.08}_{-0.08}$	1.46 $1.47^{+0.12}_{-0.12}$
07518–1354 64096	60.59 ± 0.59	...	60.2 $60.6^{+1.6}_{-1.5}$	1.001 $1.002^{+0.053}_{-0.050}$	1.93 $1.90^{+0.15}_{-0.14}$	0.97 $0.95^{+0.10}_{-0.09}$	0.97 $0.95^{+0.06}_{-0.05}$
11560+3520 103613	13.86 ± 0.58	14.73 ± 0.37	17.4 $17.1^{+1.6}_{-1.9}$	0.839 $0.841^{+0.026}_{-0.025}$	2.14 $2.25^{+0.83}_{-0.48}$	1.16 $1.22^{+0.45}_{-0.26}$	0.98 $1.03^{+0.38}_{-0.22}$
14492+1013 130669	22.6 ± 1.2	...	22.69 $22.64^{+0.31}_{-0.31}$	1.007 $1.007^{+0.019}_{-0.017}$	1.679 $1.684^{+0.060}_{-0.057}$	0.84 $0.84^{+0.03}_{-0.03}$	0.84 $0.84^{+0.03}_{-0.03}$
15282–0921 137763	48.6 ± 1.3	...	50.3 $50.7^{+2.0}_{-1.9}$	0.6731 $0.6745^{+0.0077}_{-0.0076}$	1.5024 $1.486^{+0.073}_{-0.068}$	0.90 $0.89^{+0.05}_{-0.04}$	0.60 $0.60^{+0.03}_{-0.03}$
16584+3943 153527	8.8 ± 0.68	8.97 ± 0.05	9.325 $9.313^{+0.096}_{-0.099}$	0.879 $0.879^{+0.016}_{-0.016}$	2.059 $2.065^{+0.038}_{-0.036}$	1.10 $1.10^{+0.02}_{-0.02}$	0.96 $0.97^{+0.02}_{-0.02}$
18384–0312 172088	20.85 ± 0.91	...	20.69 $20.70^{+0.12}_{-0.12}$	0.9546 $0.9539^{+0.0057}_{-0.0056}$	2.351 $2.349^{+0.024}_{-0.023}$	1.20 $1.20^{+0.01}_{-0.01}$	1.15 $1.15^{+0.01}_{-0.01}$
20102+4357 191854	19.48 ± 0.54	19.30 ± 0.13	18.04 $18.39^{+0.99}_{-0.89}$	0.65 $0.72^{+0.13}_{-0.11}$	2.12 $2.00^{+0.32}_{-0.29}$	1.29 $1.16^{+0.22}_{-0.20}$	0.84 $0.84^{+0.14}_{-0.13}$
20205+4351 193793	0.25 ± 0.42	0.538 ± 0.024	0.691 $0.648^{+0.040}_{-0.044}$	0.411 $0.413^{+0.027}_{-0.027}$	29.0 $33.6^{+4.7}_{-3.5}$	20.5 $23.7^{+3.2}_{-2.4}$	8.4 $9.9^{+1.6}_{-1.3}$
20527+4607 ...	19.0 ± 1.0	18.07 ± 0.56	18.75 $18.71^{+0.40}_{-0.41}$	0.922 $0.923^{+0.020}_{-0.020}$	2.073 $2.079^{+0.090}_{-0.083}$	1.08 $1.08^{+0.05}_{-0.04}$	1.00 $1.00^{+0.04}_{-0.04}$
23485+2539 223323	14.51 ± 0.47	14.42 ± 0.03	14.28 $14.25^{+0.45}_{-0.45}$	1.005 $1.005^{+0.014}_{-0.014}$	2.172 $2.176^{+0.026}_{-0.026}$	1.08 $1.09^{+0.01}_{-0.01}$	1.09 $1.09^{+0.01}_{-0.01}$

Note.

^a The first solution is computing an orbital parallax. The second solution is imposing the Gaia eDR3 parallax as a (Gaussian) prior to the solution. See also Figure 8 and Section 5.

0.1 ± 1.1 mas ($N=8$ objects), and -0.9 ± 1.6 mas ($N=7$ objects), respectively,²³ showing that our orbital parallaxes are indeed reliable. It is interesting to note that the rms with respect to Gaia is smaller than that with respect to Hipparcos, which indicates that at least some of the variance on this difference comes from the trigonometric parallaxes themselves and not the orbital parallaxes, as the rms is smaller for the better-quality Gaia parallaxes.

Several objects of our sample show ambiguity regarding their mass ratio; preliminary results using both the ORBIT routine and our MCMC method gave estimates of m_B/m_A in regions arbitrarily close to 1. Moreover, in most of these cases, swapping the primary and the secondary, i.e., taking observations of the RV of the primary as observations of the secondary, and vice versa, also led to valid solutions. To deal with this ambiguity, we adapted the methodology described in Mendez et al. (2017, 2021) to accept values of m_B/m_A greater than 1. While both previous studies and the present work rely on a Metropolis-within-Gibbs scheme to generate samples from the posterior distributions, the former rejects samples containing a value of m_B/m_A outside the interval (0, 1). Instead, the

method proposed here swaps RV observations whenever m_B/m_A is greater than 1 and carries out the minimum least-squares estimation of a , ω , and V_{CoM} —conditional to the rest of the parameters—in a manner akin to that explained in Mendez et al. (2017, Appendix 1). This approach produces a shift of $\pm 180^\circ$ in ω , as this parameter explicitly depends on the precedence of a binary and secondary, which is corrected in a postprocessing step.

4. H-R Diagram

In Figure 5, we present an observational H-R diagram for the six visual systems with available V and $(V-I)$ for each component. To obtain the $(V-I)$ colors, we used the V magnitudes given in Table 1 and the I magnitudes derived as explained in Section 2.1. To determine M_V , we used the published trigonometric parallaxes given in Table 4. We note that, due to the log factor, there is no significant difference if we instead use the orbital parallax. Also, at this scale, the formal error in absolute magnitude due to photometric and parallax uncertainties is negligible (of course, this does not consider possible systematic effects or biases on the parallaxes, which could be larger than the formal uncertainties). All of these systems lie at a distance of less than 65 pc; hence, we did

²³ In all of these calculations, we excluded TOK39Aa,Ab; see previous footnote.

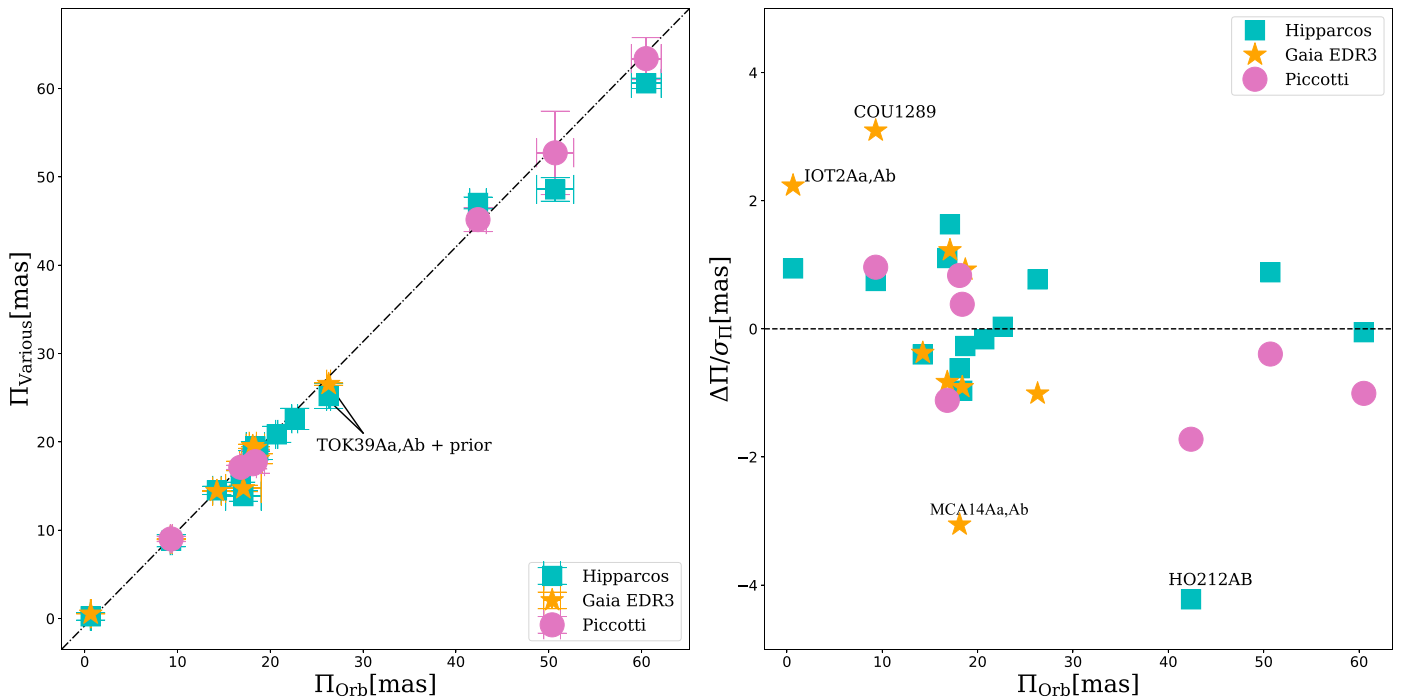


Figure 4. Comparison of trigonometric and orbital parallaxes for our sample of SB2s. The left panel shows a comparison of our orbital parallax Π_{Orb} with the Hipparcos parallax (from the re-reduction by van Leeuwen 2010), the Gaia eDR3 parallax, and the orbital parallaxes from Piccotti et al. (2020). The correlation is good and tight. The dotted–dashed line is a one-to-one relationship shown for reference. In the right panel, we plot the deviation of $(\Pi_{\text{Orb}} - \Pi_{\text{Various}})/\sigma_{\Pi}$, where σ_{Π} includes our uncertainty and those quoted for Hipparcos, Gaia, and Piccotti in Table 4. The four most discrepant cases, identified in the plot, are discussed further in Section 5.

not apply extinction or reddening correction to the apparent magnitudes and colors.

For reference, in the H-R diagram, we have superimposed a zero-age main sequence (ZAMS) from Schmidt-Kaler (1982; gold solid line, kindly provided by G. Carraro²⁴). In order to assess the current uncertainties in the stellar models, we have also superimposed isochrones from the Dartmouth Stellar Evolution Database (DSED²⁵) as described in Dotter et al. (2008), the Padova and Trieste Stellar Evolution Code (PARSEC²⁶) as described in Bressan et al. (2012), and the MESA Isochrones & Stellar Tracks (MIST²⁷) code as described in Dotter (2016). While there is an overall good agreement between all of these isochrones, the nonzero width of the main-sequence locus for the same age and metallicity shows the impact of using slightly different input physics in the models.

For the four systems that fall close to the isochrones, implying that their photometry is reliable, we have deduced their mass using the M_V and M_I versus mass relationships obtainable from the isochrones in order to make a comparison with our dynamical masses. To this end, we used the PARSEC 5 Gyr solar-metallicity isochrone, except in the case of A2801, which is better fitted by the PARSEC 9 Gyr isochrone. The comparison is shown in the table inserted in Figure 5. This exercise is obviously not meaningful in the case of the three systems that lie far from the isochrones: WDS 07518–1354 = BU101, WDS 14492+1013 = A2983, and WDS 18384–0312 = A88AB. For these, we can do a reverse process; that is, starting from the dynamical masses, we can compute the predicted photometry they should have. This

approach assumes that the published photometry is erroneous, our masses are reliable, and the theoretical predictions are accurate. The results of this exercise are shown in Figure 6. In the table inserted in this figure, we give the resulting “corrected” photometry. We believe that these discrepancies are not related to metallicity. Even though, of the three offending cases, there is published metallicity only for A2983 (with $[\text{Fe}/\text{H}] = -0.03$ according to SIMBAD), we base our conclusion on the fact that the main sequence of the PARSEC theoretical isochrones with lower metallicity cannot simultaneously fit the location on the H-R diagram of the primary and secondary in any of the cases. Further discussions are presented in the next section on a case-by-case basis.

5. Discussion of Individual Objects

Based on Figures 5 and 6 in the previous section and our orbital fitting results from Section 3, in what follows, we present comments on individual systems.

We note that six of our systems, identified below, are included in a recent paper by Piccotti et al. (2020), who compiled a list of SB2s with published astrometric orbits in order to determine the orbital parallaxes. This group, however, did not recompute orbits; using the published orbital elements, they derived orbital parallaxes assuming that the (independent) fits to the astrometric orbit and the RV were consistent. This differs substantially from our approach in that we have computed orbital elements in a dynamically self-consistent way by performing a simultaneous fit to all of the available data.

WDS 00352–0336 = HO212AB. Ours is the first combined orbit for this SB2 system in which the primary is an SB1 system (not studied here). Since the last published orbit in 2005, we have added 25 new HRCam@SOAR interferometric measurements, the most recent ones on 2018.56 and 2019.95.

²⁴ Personal communication.

²⁵ Available at http://stellar.dartmouth.edu/models/isolf_new.html.

²⁶ Available at http://stev.oapd.inaf.it/cgi-bin/cmd_3.4.

²⁷ Available at http://waps.cfa.harvard.edu/MIST/interp_isos.html.

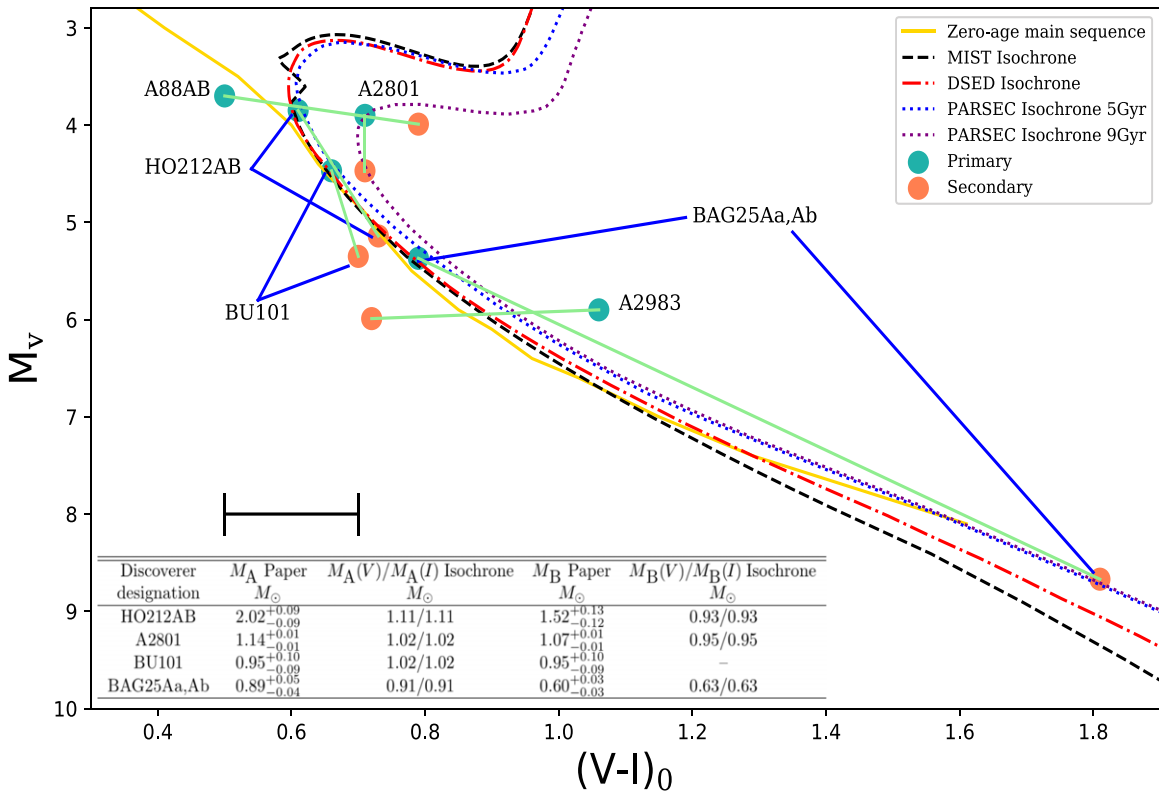


Figure 5. The H-R diagram for our sample of SB2 systems with available photometry. Green dots depict primary components, and orange dots depict the secondaries. Each pair has been linked with a line, and the discoverer designation is noted. The bar at (0.6, 8.0) shows the estimated error of the photometry, as discussed in Section 2. For reference, we have plotted an empirical ZAMS, three solar-metallicity ($Z_\odot = 0.0152$) 5 Gyr old theoretical isochrones, and a 9 Gyr isochrone. In the inserted table, we show a comparison of our estimated masses and the mass predicted by the theoretical models. See text for details and comments on individual systems.

Our orbital parallax (42.4 ± 0.9 mas) is slightly smaller than that reported by Piccotti et al. (2020; 45.2 ± 1.4 mas), but they are consistent within 2σ . Our result is, however, significantly smaller than the Hipparcos parallax at the 5σ level, not very comfortable considering that both the astrometric orbit and RV curves are quite well sampled and all of the orbital elements have small formal uncertainties. We note that a parallax from Gaia is not available yet.

As shown in Figure 4, this is actually our most extreme outlier in terms of the difference between the orbital and trigonometric parallax. In SB9, the orbit for this system is currently considered preliminary, and it was derived by keeping the period and eccentricity, which were presumably assumed from the visual orbit, fixed. In the present work, these parameters were well determined. Based on the location of both components on the H-R diagram, their photometry seems reliable. However, judging from the theoretical isochrones, their inferred masses should be significantly smaller (see table inserted in Figure 5). If we scale down the individual masses reported in Table 4 to the Hipparcos parallax instead of our orbital parallax, the individual masses become 1.49 and $1.11 M_\odot$, respectively, closer to the values inferred from the isochrones but still too large. The spectral type (F7V–F8V) for the primary implies a mass between 1.23 and $1.29 M_\odot$, while for the secondary (G4V; see Table 1), it should be $1.06 M_\odot$ (see Table 18 in Abushattal et al. 2020). These numbers are still slightly larger than the masses implied by the isochrones but more in line with the larger Hipparcos parallax than our orbital parallax. Even if we disregard the mass implied by the spectral type of the primary, we note that in general, there is a good

correspondence between the different sources of the photometry for this binary, as can be seen in Tables 1 and 2.

We conclude that the implied masses from the isochrone shown in Figure 5 are probably reliable; thus, at present, we have no explanation for the large difference between our dynamical and isochrone masses.

WDS 02128–0224 = TOK39Aa,Ab. This object is not listed in Orb6, so ours is the first astrometric orbit and also the first combined orbit. Phase coverage is excellent in RV, but astrometrically, it is rather poor; less than 50% of the orbit has been sampled, which results in a somewhat uncertain inclination of the orbit. See Table 3 and the top panel of Figure 8. As a consequence, the orbital parallax is not well determined, and the individual component masses exhibit a very large uncertainty. However, we can use the Gaia parallax as a prior in our solution (see Table 4), which leads to better-defined orbital parameters and well-constrained masses. The main impact of using this prior in the solution is a significant reduction in the uncertainty of the semimajor axis, which varied from $13.98^{+0.75}_{-0.64}$ to $14.12^{+0.15}_{-0.15}$ mas. This being a first orbit, we show the fits to this system in Figure 7, while in Figure 8, we show the PDFs without (top panel) and with (bottom panel) the use of a parallax prior. Examining the values in Table 4 and the PDFs, it is interesting to note that despite the fact that there is a significant reduction in the interquartile ranges when using a parallax prior, the ML and mid-quartiles are not that different between these two solutions; i.e., the best estimates seem to be somewhat resilient to uncertainties in the orbital fitting. Nevertheless, we expect to improve the

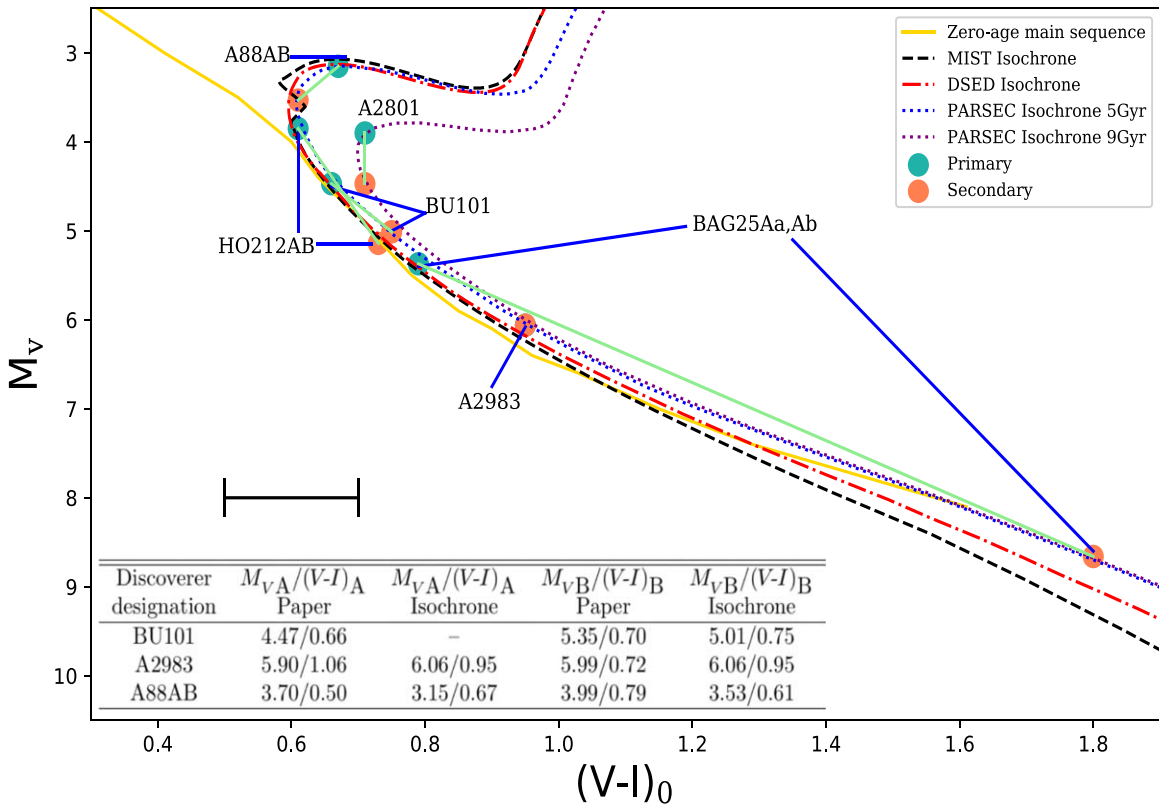


Figure 6. Same as Figure 5 but for objects with dubious photometry. Having corrected their photometry using the procedure explained in the text, we depict their putative location on the H-R diagram. The table inserted in the figure gives their measured and “corrected” photometry.

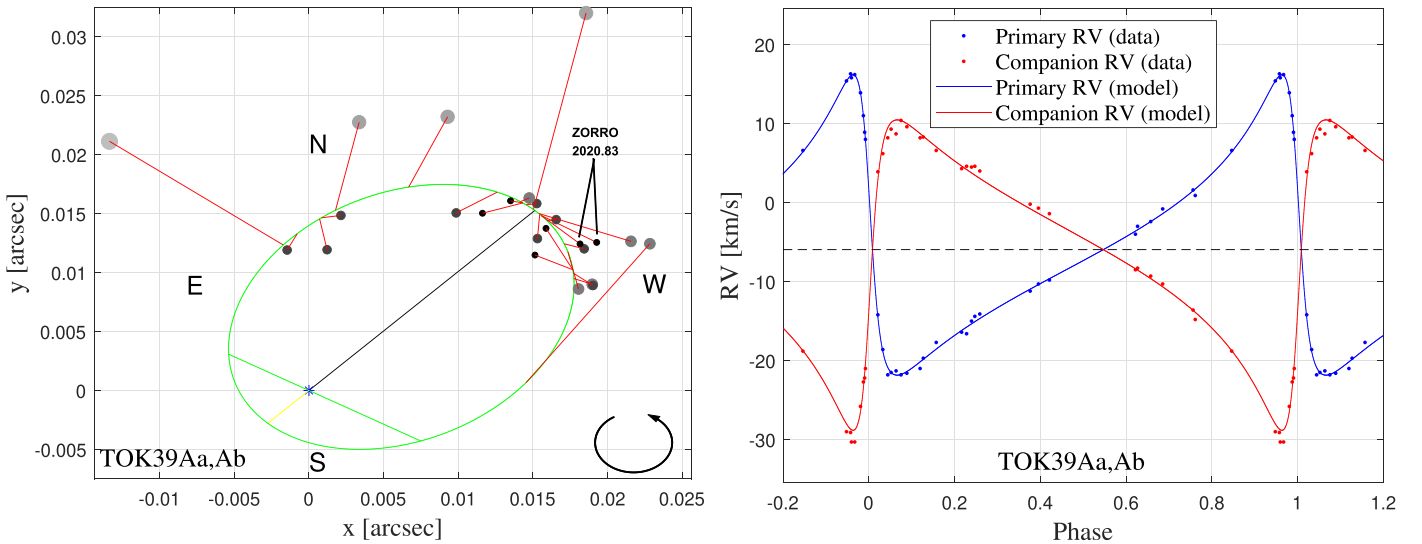


Figure 7. The ML orbit for TOK39Aa,Ab. Symbols are the same as in Figure 2. Shown is the solution without a prior. As explained in the text, if a parallax prior is used, the resulting plot is quite similar. The currently incomplete orbital coverage justifies the use of a high-precision Gaia parallax prior, which significantly improved the precision of our estimate of the individual component masses (see Figure 8).

astrometric orbit in the next few years; the most recent epochs are from our programs with HRCam@SOAR in 2020.82 and 2020.92 and ZORRO@GS²⁸ in 2020.83. Unfortunately, all of our latest observations cover the same sector of the orbit (see Figure 7). As a final note, the F8V spectral type for the primary implies a mass of $1.23 \pm 0.05 M_{\odot}$ (Abushattal et al. 2020,

Table 18), within 1σ of our dynamical mass (with prior), as shown in Table 4.

WDS 04107–0452 = A2801. The latest astrometric orbit available for this system is from Tokovinin (2017). We have added two new measurements made on 2016.96 and 2018.97 with HRCam@SOAR and obtained an orbital parallax of 16.58 ± 0.12 mas. This object is also included in Piccotti et al. (2020)’s study, which obtained an orbital parallax of 17.12 ± 0.24 mas, while a previous study from Docobo et al.

²⁸ For a description of the ZORRO instrument and its reduction pipeline, please see Howell et al. (2011), Horch et al. (2011), and Scott et al. (2018).

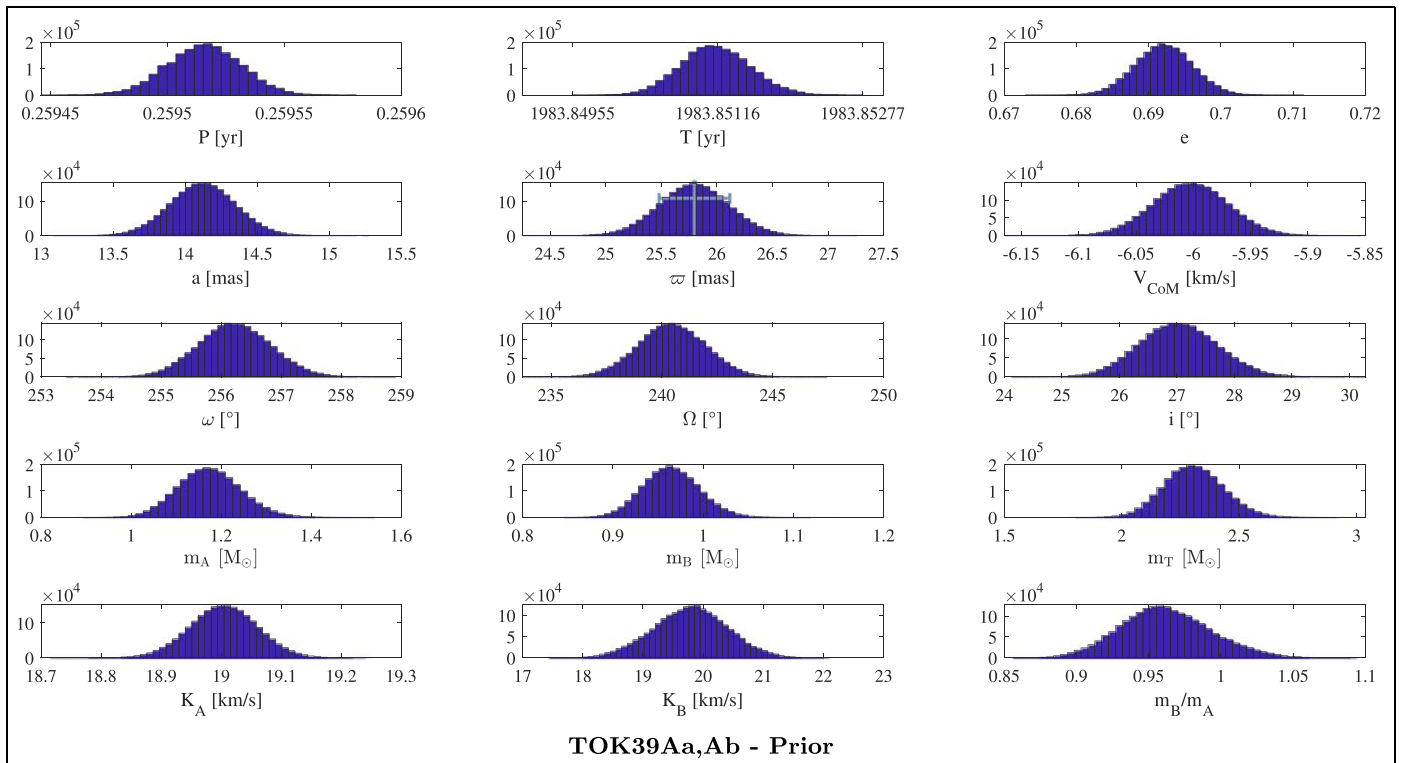
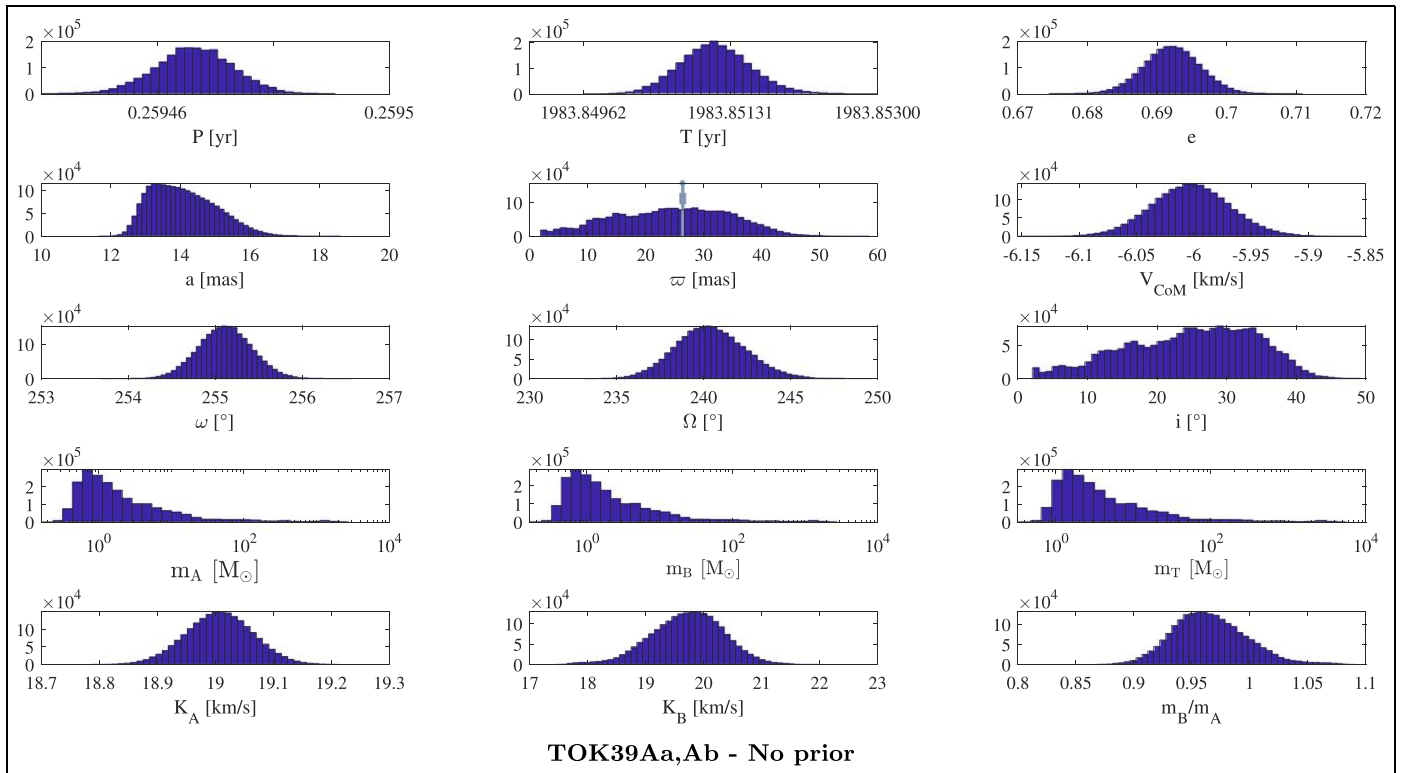


Figure 8. Posterior distribution functions for TOK39Aa,Ab. The top panel shows the solutions obtained without a parallax prior, and the bottom panel shows those obtained with a parallax prior. Note that in the top panel, the mass scale is logarithmic, while in the bottom panel, it is linear. Even in the no-prior scenario, the interquartile range and ML value for the parallax are commensurate with the Gaia eDR3 value.

(2017) gives 16.18 ± 0.23 mas. This latter value is more in line with our result.

Our derived individual component masses are quite consistent with those from Docobo et al. (2017) and Piccotti but somewhat larger than those implied by the isochrones (see

table inserted in Figure 5). If we scale our masses to the Gaia parallax instead of our orbital parallax, the individual component masses turn out to be 1.10 and $0.98 M_\odot$, respectively, quite close to those from the isochrones. However, the spectral type of the primary (G0IV–G5IV)

implies a mass between 1.26 and $1.20 M_{\odot}$ (see Table 19 in Abushattal et al. 2020), closer to the masses derived from our orbital parallax. The photometry suggests that the primary is leaving the main sequence; in our H-R diagrams, the isochrone that best fits both components is the PARSEC 9 Gyr (see Figure 5). This is consistent with the luminosity class IV given for the primary in SIMBAD (see Table 1).

WDS 04184+2135 = MCA14Aa,Ab. This is a reanalysis of an orbit already studied by Torres et al. (1997), who derived a combined spectroscopic and astrometric solution yielding an orbital parallax of 17.92 ± 0.58 mas and masses of 1.80 ± 0.13 and $1.46 \pm 0.18 M_{\odot}$ for the primary and secondary, respectively. More recently, Pourbaix (2000) also obtained a combined solution for this resolved SB2, yielding orbital parallaxes and component masses similar to those derived by Torres and collaborators. After these studies, five new astrometric observations of this system were secured between 1997.14 and 2005.86 using 4 m facilities with adaptive optics and speckle imaging, and we included them in our reanalysis. Our derived orbital parallax is slightly larger, at 18.16 ± 0.39 mas, but our individual masses are basically the same as those from Torres et al. (1997). We note that the Gaia eDR3 trigonometric parallax is larger than ours by almost 3σ (see Figure 4). Piccotti et al. (2020) gave an orbital parallax of 17.55 ± 0.59 mas, even more discrepant with the Gaia eDR3 value, but their derived masses are not so discrepant from ours: 1.87 ± 0.58 and $1.52 \pm 0.19 M_{\odot}$. Our formal errors are, however, significantly smaller (see Table 4). Given the spectral type of the primary (F0V), Abushattal et al. (2020) predicted a mass of $1.64 \pm 0.05 M_{\odot}$ for it, which differs by less than 1σ of our dynamical mass.

WDS 07518-1354 = BU101. We have included this well-studied equal-mass binary as a benchmark to compare literature values with our results. The result reported in SB9 comes from a combined astrometric and spectroscopic orbit by Pourbaix (2000). The visual orbit was subsequently revised by Tokovinin (2012) using newer astrometric observations made with HRCam@SOAR. Our solution incorporates more recent measurements made with the same setup,²⁹ 2019.95 being our last epoch. Our orbital parameters are in agreement with those from Tokovinin, albeit with smaller formal uncertainties on account of the incorporation of new data. Given its photometry, the mass of the primary is in very good agreement with the prediction from the isochrones (see table inserted in Figure 5), but the secondary is off, which casts some doubts on the photometry of the latter. In Figure 6, which includes the photometry in the inserted table, we show the location that the secondary should have had given its empirical mass and isochrones. The difference between the measured and expected magnitudes in V is 0.34 mag, which is quite large, but in color, the difference is smaller, 0.05 mag. Also note that the V -band photometry for this target does not exhibit such a large variance according to Tables 1 and 2. Our individual masses seem more consistent with a G7V–G8V spectral type (according to Abushattal et al. 2020, their Table 18), rather than the earlier types given in WDS (G0V) and SIMBAD (G1V), which imply larger masses. However, given our 10% mass uncertainty, the earlier types are consistent within 1σ of our mass interquartile range (see Table 4). We finally note that

Piccotti et al. (2020) reported an orbital parallax of 64.4 ± 2.4 mas, which is within 1.5σ of our value of 60.2 ± 1.5 mas, and the same happens with the individual component masses. Perhaps the most intriguing aspect of this binary is that, despite the fact that both components have the same mass (within the errors), their photometry seems to indicate different locations for them on the H-R diagram, which should not be the case if they are coeval. Note, e.g., the good correspondence between ΔV and the Δy value given in Table 1, which shows that they do not seem to have the same luminosity.

WDS 11560+3520 = CHR258. Ours is the first combined orbit for the external pair of this triple hierarchical system. The formal uncertainty of the orbital parallax (1.9 mas) is significantly worse than the uncertainties of the trigonometric parallaxes from Hipparcos (0.58 mas) and Gaia eDR3 (0.37 mas). This is most likely due to the poor orbital coverage; only three astrometric points are available, but they are well distributed in the orbit. An alternative solution, using a fixed parallax at the eDR3 value, leads to larger individual component masses of 1.84 and $1.53 M_{\odot}$, in accordance with the smaller system’s parallax. The spectral type (F5), however, implies a mass of $1.39 \pm 0.05 M_{\odot}$ (Abushattal et al. 2020), in agreement with our value of $1.22^{+0.45}_{-0.26} M_{\odot}$, thus somewhat validating our larger orbital parallax. This is an interesting system that deserves further astrometric observations of the external pair for better orbital coverage. The phase coverage on the RV curve is already quite good.

WDS 14492+1013 = A2983. The latest visual orbit included in Orb6 is that from Docobo et al. (2018a), but more recently, Al-Tawalbeh et al. (2021) revised this solution and obtained a system mass of $1.61 \pm 0.26 M_{\odot}$ and an orbital parallax of 21.81 ± 0.8 mas. These results lie within 1σ of our derived values, but our combined solution yields much smaller formal uncertainties, due in part to our combined solution and also to the addition of three new HRCam+SOAR measurements in 2018.16, 2019.14, and 2019.54. The mass implied by the spectral type of the primary (K2V) is $0.80 \pm 0.03 M_{\odot}$ (Abushattal et al. 2020), in very good agreement with our dynamical mass. Griffin (2015) reported $m_A \sin^3 i = 0.308 \pm 0.012$ and $m_B \sin^3 i = 0.306 \pm 0.011 M_{\odot}$ for this object, which for our value of the inclination (see Table 3) implies masses of 0.898 and $0.892 M_{\odot}$, consistent at the 1σ level with our determination shown in Table 4. As can be seen in Figure 5, the measured photometry, however, seems at odds with its location on the H-R diagram, in particular regarding the large $\Delta I = 0.43 \pm 0.12$ mag given in Table 1. In Figure 6, we show the location it should have on the H-R diagram on account of its mass; because it is an equal-mass binary, the primary and secondary are located on the same point of the isochrone.

WDS 15282-0921 = BAG25Aa,Ab. This is the first combined orbit for this highly eccentric SB2 inner pair of a triple system. Piccotti et al. (2020) gave masses of 0.84 ± 0.30 and $0.58 \pm 0.21 M_{\odot}$ and an orbital parallax of 52.7 ± 4.7 mas. Our orbital parallax is smaller and more in line with the Hipparcos parallax (no Gaia parallax for this object yet), with formal errors a factor of 2 smaller in orbital parallax and a factor of 6 improvement in the individual masses. This is mostly due to the fact that, since the last published orbit in Orb6 from Tokovinin (2016), our survey has added seven high-precision observations from HRCam@SOAR, the latest being on 2019.14. The

²⁹ Actually, this binary is observed frequently as an “astrometric standard” because it is used to calibrate the plate scale and orientation of HRCam; see Section 3.

photometry seems reliable; all measurements in Tables 1 and 2 agree within the uncertainties. As shown in the table inserted in Figure 5, our orbital masses agree very well with the theoretical masses for both the primary and secondary. Based on the spectral type (G9V) of the primary, Abushattal et al. (2020) predicted a mass of $0.93 \pm 0.04 M_{\odot}$, consistent with our reported value of $0.89^{+0.05}_{-0.04} M_{\odot}$.

WDS 16584+3943 = COUI289. Ours is the first combined orbit for this system. Piccotti et al. (2020) obtained an orbital parallax of 9.00 ± 0.30 mas, slightly smaller than ours (but within 1σ) and more in line with the Gaia eDR3 value. Their individual masses are also within 1σ with ours, but our formal errors are much smaller. No new observations were incorporated into our solution, just the data used in the original visual orbit by Docobo & Ling (2013) and the spectroscopic orbit from Griffin (2003). The differences in uncertainty with respect to the Piccotti result are likely a consequence of the better performance of the self-consistent simultaneous combined fit. Given the small errors of both the Gaia parallax and our orbital parallax, the difference of 0.36 mas seems uncomfortably large (see Figure 4). Note that the RV curve covers the range 0.9–1.1 in phase with no data at intermediate phases, while almost the opposite happens in the case of the astrometric curve, which may be the culprit for a somewhat uncertain orbital parallax. If we assume the primary is a G0V, its M_V is +4.40 (Abushattal et al. 2020, their Table 18), which for the Gaia parallax (see Table 4) implies a primary $V = 9.64$. If we assume a nearly equal-mass system, consistent with our results given in Table 4 and the $\Delta V = 0$ reported by WDS, then the system’s magnitude will be $V = 8.88$, which is significantly fainter than the magnitude predicted by WDS (7.65 mag) and also fainter than the Hipparcos measurement (8.09 mag). Incidentally, ASAS-SN reports $V = 8.52 \pm 0.094$, but this value is uncertain due to the bright limit at $V = 10$ of this survey. We have no explanation for this discrepancy on the photometry.

WDS 18384–0312 = A88AB. This is the first combined orbit. It has a very tight fit with good orbital and phase coverage. Our results are in agreement with those from Malkov et al. (2012), who obtained a dynamical mass for the pair of $2.42 \pm 0.32 M_{\odot}$. On the other hand, Griffin (2013b) obtained $m_A \sin^3 i = 0.690 \pm 0.013$ and $m_B \sin^3 i = 0.660 \pm 0.012 M_{\odot}$ from the RV alone, which, for our value of the inclination (see Table 3), implies masses of 1.75 and 1.15 M_{\odot} . The mass for the primary is significantly larger than ours (1.20 M_{\odot}), whereas the mass of the secondary is totally consistent with our result. Given the spectral type of the primary, F8V–F9V, the implied mass (Abushattal et al. 2020) is 1.23–1.20 M_{\odot} , which coincides well with our value.

We note that since the last visual orbit published for this binary in 2013, eight new interferometric observations have been made: two on 2014.76 by Horch et al. (2015a) with the 4.3 m Discovery Channel Telescope and six by us with the HRCam@SOAR program between 2015.50 and 2019.61.

As result, both the RV curve and the astrometric orbit are now very well sampled, and our orbital parameters and derived masses are tight. There is no Gaia parallax yet for this target, but our orbital parallax coincides within 1σ with the Hipparcos parallax. As was the case for A2983, the measured photometry seems at odds with its location on the H-R diagram (see Figure 5). As before, in Figure 6, we show the location it should have on the H-R diagram given its mass, together with the photometry in the inserted table. If we assume a typical age

for disk stars of 5 Gyr, this location implies that it may be a slightly evolved system.

WDS 20102+4357 = STT400. A first combined orbit was published by Pourbaix (2000). In our solution, we have included 12 new interferometric observations carried out in the period 2000.20–2013.83 by various authors, which improved the orbital coverage. We note that the orbit is not yet complete because of the period, which is nearly 85 yr. At this point, the combined solution is limited mostly by the small phase coverage in the RV curve. Piccotti et al. (2020) gave 17.8 ± 1.3 mas for the orbital parallax and masses of 1.24 ± 0.38 and $0.96 \pm 0.26 M_{\odot}$, similar to our values. There are spectral types for both the primary (G3V–G4V) and secondary (G8V), indicating a mass of $1.07\text{--}1.06 \pm 0.04 M_{\odot}$ (Abushattal et al. 2020), that compare well with our values within our rather large mass uncertainties of 0.1–0.2 M_{\odot} for this system.

WDS 20205+4351 = IOT2Aa,Ab. We selected this interesting target because of its small, and hence uncertain, trigonometric parallax (even for Gaia). On the other hand, in principle, our orbital parallaxes are distance-independent. The O-type + WR pair has been studied by Monnier et al. (2011), who derived masses of 35.9 ± 1.3 and $14.9 \pm 0.5 M_{\odot}$ for a distance of 1.76 ± 0.03 kpc, i.e., a parallax of 0.57 ± 0.01 mas. The latest Gaia eDR3 parallax is 0.538 ± 0.069 mas (see Table 4), consistent within 1.5σ with the Monnier et al. (2011) value. Our estimated orbital parallax is larger than the previous values, implying smaller component masses of 20.5 ± 3.2 and $8.4 \pm 1.6 M_{\odot}$. The precision on our orbital parallax is, however, a factor of 2 worse than that from Gaia (see Figure 4), probably due to the combination of the rather poor orbital coverage with the noisy RV of the early-type stars involved.³⁰ Scaling our parallax to that of Monnier et al. (2011) would imply masses of 36.5 and 15.0 M_{\odot} , more in line with their results. Unfortunately, our attempt to use this system as a test case for the orbital parallaxes is not conclusive, not due to a fundamental limitation of our methodology but rather to the limited coverage and the quality of the observational data.

WDS 20527+4607 = A750. Ours is the first combined orbit. The visual orbit only encompasses about 50% of the orbit, but the combined solution looks solid, with small uncertainties. Our orbital parallax coincides within 1σ with the Gaia eDR3 result, while the individual component masses have a 4% uncertainty. We have obtained $1.08 \pm 0.05 M_{\odot}$ for the mass of the primary, which coincides reasonably well with that predicted by Abushattal et al. (2020) from the G8V spectral type of the primary ($0.96 \pm 0.04 M_{\odot}$).

WDS 23485+2539 = DSG8. Ours is the first fully self-consistent orbit. Horch et al. (2019b) provided orbital elements by fitting the RV curve independently from the visual orbit obtained using Tokovinin’s ORBIT code (see Table 5 in Horch et al. 2019b). They obtained an orbital parallax of 14.3 ± 0.4 mas, similar to our value, and likewise with the masses that have very small uncertainties. At $\sim F5V$, the WDS spectral types of the primary and secondary imply a large mass of 1.35 M_{\odot} (Abushattal et al. 2020). SIMBAD gives a spectral type of F2IV–V, indicating even larger masses. This discrepancy is probably due to the low metallicity of the system ($[Fe/H] = -0.46$), which makes the spectral type of the system seem earlier than it really is.

³⁰ See the RV fits at http://www.das.uchile.cl/~rmendez/B_Research/JAA-RAM-SB2/.

6. Conclusions

We have done a thorough search of Orb6 (Mason et al. 2001) and SB9 (Pourbaix et al. 2004) looking for SB2s lacking a published combined visual and spectroscopic orbit. We found eight systems that met this condition: WDS00352–0336 = HO212AB, WDS02128–0224 = TOK39Aa, Ab, WDS11560+3520 = CHR258, WDS15282–0921 = BAG25Aa,Ab, WDS16584+3943 = COU1289, WDS18384–0312 = A88AB, WDS20527+4607 = A750, and WDS23485+2539 = DSG8. One of these pairs, TOK39Aa,Ab, also did not have a visual orbit.

Using an MCMC code developed by our group, we carried out dynamically self-consistent simultaneous fits to the data, obtaining orbital elements, individual component masses, and orbital parallaxes. A comparison of our orbital parallaxes with trigonometric parallaxes from Hipparcos and Gaia shows a generally good agreement.

We also computed joint solutions for six comparison binaries: WDS04107–0452 = A2801, WDS 04184+2135 = MCA14Aa,Ab, WDS07518–1354 = BU101, WDS14492+1013 = A2983, WDS20102+4357 = STT400, and WDS20205+4351 = IOT2Aa,Ab. Even in these cases, we could improve the previous orbits by adding recent data from our speckle survey of binaries being carried out with HRCam@SOAR and ZORRO@GS.

The mass ratios could be determined in the best cases with less than 1% uncertainty, while the uncertainty on the mass sum is about 1%. The formal uncertainty of the best individual component masses that we could determine is $0.01 M_{\odot}$. We have placed those objects that have individual component photometry on an H-R diagram to compare their location in relation to various theoretical isochrones and an empirical ZAMS. We also provide a detailed discussion of our results on an object-by-object basis.

We are very grateful to the referee for a careful reading of our manuscript and the many detailed suggestions that have improved the readability of the text.

J.A.A., R.A.M., and E.C. acknowledge support from ANID/FONDECYT grant No. 1190038.

We are grateful to Andrei Tokovinin (CTIO/NOIRLab) for his help and support in the use of HRCam at SOAR and to Ricardo Salinas (GS/ZORRO instrument scientist), Elise Furlan (scientist, NASA Exoplanet Science Institute Caltech/IPAC), and Steve Howell (scientist, Space Science and Astrobiology Division, NASA Ames Research Center) for their help and support in the use of ZORRO at Gemini South. We also acknowledge all of the support personnel at CTIO and GS for their commitment to operations during these difficult COVID times.

This research has made use of the Washington Double Star Catalog, maintained at the U.S. Naval Observatory, and the SIMBAD database, operated at CDS, Strasbourg, France. This research was made possible through the use of the AAVSO Photometric All-Sky Survey (APASS), funded by the Robert Martin Ayers Sciences Fund and NSF AST-1412587. This work has made use of data from the European Space Agency (ESA) mission Gaia (<https://www.cosmos.esa.int/gaia>), processed by the Gaia Data Processing and Analysis Consortium (DPAC; <https://www.cosmos.esa.int/web/gaia/dpac/consortium>). Funding for the DPAC has been provided by national institutions, in particular the institutions participating in the

Gaia Multilateral Agreement. We are very grateful for the continuous support of the Chilean National Time Allocation Committee under programs CN2018A-1, CN2019A-2, CN2019B-13, CN2020A-19, CN2020B-10, and CN2021B-17 for SOAR and the Gemini Time Allocation Committee under program IDs GS-2019A-Q-110, GS-2019A-Q-311, GS-2019B-Q-116, GS-2019B-Q-223, GS-2020A-Q-116, and GS-2020B-Q-142.

Some of the observations in this paper made use of the high-resolution imaging instrument ZORRO. ZORRO was funded by the NASA Exoplanet Exploration Program and built at the NASA Ames Research Center by Steve B. Howell, Nic Scott, Elliott P. Horch, and Emmett Quigley. ZORRO is mounted on the Gemini South telescope of the international Gemini Observatory, a program of NSF's NOIRLab, which is managed by the Association of Universities for Research in Astronomy (AURA) under a cooperative agreement with the National Science Foundation on behalf of the Gemini Observatory partnership: the National Science Foundation (United States), National Research Council (Canada), Agencia Nacional de Investigación y Desarrollo (Chile), Ministerio de Ciencia, Tecnología e Innovación (Argentina), Ministério da Ciência, Tecnologia, Inovações e Comunicações (Brazil), and Korea Astronomy and Space Science Institute (Republic of Korea).

We humbly dedicate this work to the memory of Dr. Dimitri Pourbaix, a lead researcher in the field of binary star research and principal author and keeper of the SB9 catalog, without which this work would not have been possible. His sudden death on 2021 November 14 is a great loss to our field, and he will be sorely missed by all of us.

ORCID iDs

Rene A. Mendez  <https://orcid.org/0000-0003-1454-0596>

References

- Abushattal, A. A., Docobo, J. A., & Campo, P. P. 2020, *AJ*, **159**, 28
- Al-Tawalbeh, Y. M., Hussein, A. M., Taani, A. A., et al. 2021, *AstBu*, **76**, 71
- Benedict, G. F., Henry, T. J., Franz, O. G., et al. 2016, *AJ*, **152**, 141
- Bennett, D. P., Bhattacharya, A., Beaulieu, J.-P., et al. 2020, *AJ*, **159**, 68
- Boyajian, T. S., McAlister, H. A., van Belle, G., et al. 2012a, *ApJ*, **746**, 101
- Boyajian, T. S., von Braun, K., van Belle, G., et al. 2012b, *ApJ*, **757**, 112
- Brandt, T. D. 2021, *ApJS*, **254**, 42
- Bressan, A., Marigo, P., Girardi, L., et al. 2012, *MNRAS*, **427**, 127
- Claveria, R. M., Mendez, R. A., Silva, J. F., & Orchard, M. E. 2019, *PASP*, **131**, 084502
- Cournoyer-Cloutier, C., Tran, A., Lewis, S., et al. 2021, *MNRAS*, **501**, 4464
- Docobo, J. A., & Campo, P. 2013, in IAU Comm. 26 Inform. Circular (IAUDS), Vol. 180 (Cambridge: Cambridge Univ. Press), 2
- Docobo, J. A., Campo, P., & Abushattal, A. 2018a, in IAU Comm. 26 Inform. Circular (IAUDS), Vol. 196 (Cambridge: Cambridge Univ. Press), 1
- Docobo, J. A., Campo, P. P., Gomez, J., & Horch, E. P. 2018b, *AJ*, **156**, 185
- Docobo, J. A., Gomez, J., Campo, P. P., et al. 2019, *MNRAS*, **482**, 4096
- Docobo, J. A., Griffin, R. F., Campo, P. P., & Abushattal, A. A. 2017, *MNRAS*, **469**, 1096
- Docobo, J. A., & Ling, J. F. 2013, in IAU Comm. 26 Inform. Circular (IAUDS), Vol. 180 (Cambridge: Cambridge Univ. Press), 2
- Docobo, J. A., Tamazian, V. S., Campo, P. P., & Piccotti, L. 2018c, *AJ*, **156**, 85
- Dotter, A. 2016, *ApJS*, **222**, 11
- Dotter, A., Chaboyer, B., Jevremović, D., et al. 2008, *ApJS*, **178**, 89
- Ducati, J. R., Penteadó, E. M., & Turcati, R. 2011, *A&A*, **525**, A26
- Duchêne, G. 2010, *ApJL*, **709**, L114
- Duchêne, G., & Kraus, A. 2013, *ARA&A*, **51**, 269
- Duquenois, A., & Mayor, M. 1991, *A&A*, **248**, 485
- Dvorak, R. 1982, *OAWMN*, **191**, 423
- Eddington, A. S. 1924, *MNRAS*, **84**, 308
- El-Badry, K., Rix, H.-W., & Heintz, T. M. 2021, *MNRAS*, **506**, 2269

- Feiden, G. A., & Chaboyer, B. 2012, *ApJ*, **757**, 42
- Fontanive, C., & Bardalez Gagliuffi, D. 2021, *FrASS*, **8**, 16
- Fuhrmann, K., Chini, R., Kaderhandt, L., & Chen, Z. 2017, *ApJ*, **836**, 139
- Ghosh, H., DePoy, D. L., Gal-Yam, A., et al. 2004, *ApJ*, **615**, 450
- Gómez, J., Docobo, J. A., Campo, P. P., et al. 2021, *MNRAS*, **152**, 12
- Gomez, J., Docobo, J. A., Campo, P. P., & Mendez, R. A. 2016, *AJ*, **152**, 216
- Gould, A. 2014, *JKAS*, **47**, 215
- Griffin, R. F. 1984, *Obs*, **104**, 143
- Griffin, R. F. 2003, *Obs*, **123**, 301
- Griffin, R. F. 2007, *Obs*, **127**, 113
- Griffin, R. F. 2013a, *Obs*, **133**, 322
- Griffin, R. F. 2013b, *Obs*, **133**, 269
- Griffin, R. F. 2015, *Obs*, **135**, 193
- Griffin, R. F., & Mason, B. D. 2013, in IAU Comm. 26 Inform. Circular (IAUDS), Vol. 181 (Cambridge: Cambridge Univ. Press), 1
- Halbwachs, J. L., Kiefer, F., Lebreton, Y., et al. 2020, *MNRAS*, **496**, 1355
- Halbwachs, J. L., Mayor, M., & Udry, S. 2018, *A&A*, **619**, 16
- Hatzes, A. P., Cochran, W. D., Endl, M., et al. 2003, *ApJ*, **599**, 1383
- Heintz, W. 1997, *AJ*, **111**, 335
- Henden, A. A., Welch, D. L., Terrell, D., & Levine, S. E. 2009, *BAAS*, **41**, 669
- Horch, E. P., Gomez, S. C., Sherry, W. H., et al. 2011, *AJ*, **141**, 45
- Horch, E. P., Tokovinin, A., Weiss, S. A., et al. 2019a, *AJ*, **157**, 56
- Horch, E. P., Tokovinin, A., Weiss, S. A., et al. 2019b, *AJ*, **157**, 56H
- Horch, E. P., van Altena, W. F., Demarque, P., et al. 2015b, *AJ*, **149**, 151
- Horch, E. P., van Belle, G. T., Davidson, J. W. J., et al. 2015a, *AJ*, **150**, 151
- Howell, S. B., Everett, M. E., Sherry, W., Horch, E., & Ciardi, D. R. 2011, *AJ*, **142**, 19
- Iben, I. 2012, *Stellar Evolution Physics* (Cambridge: Cambridge Univ. Press)
- Jayasinghe, T., Stanek, K. Z., Kochanek, C. S., et al. 2019, *MNRAS*, **485**, 961
- Kahler, H. 1972, *A&A*, **20**, 105
- Kervella, P., Arenou, F., Mignard, F., & Thévenin, F. 2019, *A&A*, **623**, A72
- Kippenhahn, R., Weigert, A., & Weiss, A. 2012, *Stellar Structure and Evolution* (Berlin: Springer)
- Kochanek, C. S., Shappee, B. J., Stanek, K. Z., et al. 2017, *PASP*, **129**, 104502
- Lindgren, L., Mignard, F., Söderhjelm, S., et al. 1997, *A&A*, **323**, L53
- Luri, X., Brown, A. G. A., Sarro, L. M., et al. 2018, *A&A*, **616**, A9
- Maíz Apellániz, J. 2017, *A&A*, **608**, L8
- Malkov, O. Y., Tamazian, V. S., Docobo, J. A., & Chulkov, D. A. 2012, *A&A*, **546**, A69
- Wyrzykowski, Ł., & Mandel, I. 2020, *A&A*, **636**, A20
- Mann, A. W., Dupuy, T., Kraus, A. L., et al. 2019, *ApJ*, **871**, 63
- Marchenko, S. V., Moffat, A. F. J., Ballereau, D., et al. 2003, *ApJ*, **596**, 1295
- Mason, B., Pentead, E., & Hartkopf, W. I. 2005, *IAUDS*, **156**, 1M
- Mason, B. D. 2015, *IAUGA*, **29**, 2300709
- Mason, B. D., Wycoff, G. L., Hartkopf, W. I., Douglass, G. G., & Worley, C. E. 2001, *AJ*, **122**, 3466
- Massey, P., & Meyer, M. 2001, in *Encyclopedia of Astronomy and Astrophysics*, ed. P. Murdin (Bristol: Institute of Physics Publishing), 1882
- Matson, R. A., Howell, S. B., Horch, E. P., & Everett, M. E. 2018, *AJ*, **156**, 31
- Mendez, R. A., Clavería, R. M., & Costa, E. 2021, *AJ*, **161**, 155
- Mendez, R. A., Clavería, R. M., Orchard, M. E., & Silva, J. F. 2017, *AJ*, **154**, 187
- Mendez, R. A., Tokovinin, A., & Horch, E. 2018, *RMxAA*, **50**, 56
- Monnier, J., Zhao, M., Pedretti, E., et al. 2011, *ApJ*, **742**, 6
- Mordasini, C., Alibert, Y., Benz, W., & Naef, D. 2008, in *ASP Conf. Ser.* 398, *Extreme Solar Systems*, ed. D. Fischer et al. (San Francisco, CA: ASP), 235
- Nordström, B., Mayor, M., Andersen, J., et al. 2004, *A&A*, **418**, 989
- Pegues, J., Czekala, I., Andrews, S. M., et al. 2021, *ApJ*, **908**, 42
- Piccotti, L., Docobo, J. A., Carini, R., et al. 2020, *MNRAS*, **492**, 2709
- Pickles, A., & Depagne, É. 2010, *PASP*, **122**, 1437
- Pojmanski, G. 1997, *AcA*, **47**, 467
- Pourbaix, D. 1994, *A&A*, **290**, 682
- Pourbaix, D. 2000, *A&AS*, **145**, 215
- Pourbaix, D., Tokovinin, A. A., Batten, A. H., et al. 2004, *A&A*, **424**, 727
- Queloz, D., Mayor, M., Weber, L., et al. 2000, *A&A*, **354**, 99
- Raghavan, D., McAlister, H. A., Henry, T. J., et al. 2010, *ApJS*, **190**, 1
- Riello, M., de Angeli, F., Evans, D. W., et al. 2021, *A&A*, **649**, A3
- Schmidt-Kaler, T. 1982, *Landolt-Börnstein: Numerical Data and Functional Relationships in Science and Technology*, Vol. 2 (Berlin: Springer), 19
- Scott, N. J., Howell, S. B., Horch, E. P., & Everett, M. E. 2018, *PASP*, **130**, 054502
- Söderhjelm, S. 1999, *A&A*, **341**, 121
- Thebault, P., & Haghighipour, N. 2015, in *Planet Formation in Binaries*, ed. S. Jin, N. Haghighipour, & W.-H. Ip (Berlin: Springer), 309
- Tokovinin, A. 1992, in *ASP Conf. Ser.* 32, *IAU Colloq. 135: Complementary Approaches to Double and Multiple Star Research*, ed. H. A. McAlister & W. I. Hartkopf (San Francisco, Ca: ASP), 573
- Tokovinin, A. 2012, *AJ*, **144**, 11
- Tokovinin, A. 2016, *AJ*, **152**, 9
- Tokovinin, A. 2017, *AJ*, **154**, 110
- Tokovinin, A. 2018, *PASP*, **130**, 035002
- Tokovinin, A., & Cantarutti, R. 2008, *PASP*, **120**, 170
- Tokovinin, A., & Latham, D. W. 2017, *ApJ*, **838**, 54
- Tokovinin, A., Mason, B. D., & Hartkopf, W. I. 2010, *AJ*, **139**, 743
- Torres, G., Andersen, J., & Giménez, A. 2010, *A&ARv*, **18**, 67
- Torres, G., Stefanik, R. P., & Latham, D. W. 1997, *ApJ*, **474**, 256
- van Leeuwen, F. 2010, *SSRv*, **151**, 209
- Villegas, C., Mendez, R. A., Silva, J. F., & Orchard, M. E. 2021, *PASP*, **133**, 074501
- Wall, J. E., McMillan, S. L. W., Mac Low, M.-M., Klessen, R. S., & Portegies Zwart, S. 2019, *ApJ*, **887**, 62
- Wand, M. P., & Jones, M. C. 1994, *Kernel Smoothing* (Boca Raton, FL: CRC Press)
- Wenger, M., Ochsenein, F., Egret, D., et al. 2000, *A&AS*, **143**, 9
- Ziegler, C., Law, N. M., Baranec, C., et al. 2018, *AJ*, **156**, 259